Simulation of organics in the atmosphere: evaluation of EMACv2.54 with the Mainz Organic Mechanism (MOM) coupled to the ORACLE (v1.0) submodel

Andrea Pozzer[1], Simon F. Reifenberg[1], Vinod Kumar[1], Bruno Franco[2], Matthias Kohl[1], Domenico Taraborrelli[3], Sergey Gromov[1], Sebastian Ehrhart[1], Patrick Jöckel[4], Rolf Sander[1], Veronica Fall[5], Simon Rosanka[3], Vlassis Karydis[3], Dimitris Akritidis[6], Tamara Emmerichs[3], Monica Crippa[7], Diego Guizzardi[7], Johannes W. Kaiser[8], Lieven Clarisse[2], Astrid Kiendler-Scharr[3], Holger Tost[9], and Alexandra Tsimpidi[3,10]

[1]Atmospheric Chemistry Department, Max Planck Institute for Chemistry, Mainz, Germany
[2]Université libre de Bruxelles (ULB), Spectroscopy, Quantum Chemistry and Atmospheric Remote Sensing (SQUARES), Brussels, Belgium
[3]Institute of Energy and Climate Research, IEK-8: Troposphere, Forschungszentrum Jülich GmbH, 52428 Jülich, Germany
[4]Deutsches Zentrum für Luft- und Raumfahrt (DLR), Institut für Physik der Atmosphäre, Oberpfaffenhofen, Germany
[5]Illinois-Indiana Sea Grant, University of Illinois, Champaign, IL, USA
[6]Department of Meteorology and Climatology, School of Geology, Aristotle University of Thessaloniki, Thessaloniki, Greece
[7]European Commission, Joint Research Centre, Ispra (VA), Italy
[8]Satellite-based Climate Monitoring Unit, Deutscher Wetterdienst (DWD), Offenbach am Main, Germany
[9]Institute for Atmospheric Physics, Johannes Gutenberg University, Mainz, Germany
[10]National Observatory of Athens, Inst. for Environmental Research and Sustainable Development, Athens, 15236, Greece

Correspondence: andrea.pozzer@mpic.de

Abstract. An updated and expanded representation of organics in the chemistry general circulation model EMAC (ECHAM5/MESSy for Atmospheric Chemistry) has been evaluated. First, the comprehensive Mainz Organic Mechanism (MOM) in the submodel MECCA (Module Efficiently Calculating the Chemistry of the Atmosphere) was activated with explicit degradation of organic species up to five carbon atoms and a simplified mechanism for larger molecules. Second, the ORACLE submodel (version 1.0) considers now condensation on aerosols for all organics in the mechanism. Parameterizations for aerosol yields are used only for the lumped species that are not included in the explicit mechanism. The simultaneous usage of MOM and ORACLE allows an efficient estimation, not only of the chemical degradation of the simulated volatile organic compounds, but also of the contribution of organics to the growth and fate of (organic) aerosol, with a complexity of the mechanism largely increased compared to EMAC simulations with more simplified chemistry. The model evaluation presented here reveals that the OH concentration is well reproduced globally, while significant biases for observed oxygenated organics are present. We also investigate the general properties of the aerosols and their composition, showing that the more sophisticated and process-oriented secondary aerosol formation does not degrade the good agreement of previous model configurations with observations at the surface, allowing further research in the field of gas-aerosol interactions.

1 Introduction

Volatile organic compounds (VOCs) play a pivotal role in the atmosphere by constraining the total oxidant level and serve as precursors of ozone (O_3), carbon dioxide (CO_2) and secondary organic aerosols (Heald and Kroll, 2020). Due to the complexity of the chemistry of VOCs, a comprehensive and explicit representation thereof is mostly still missing in global and regional model simulations (Heald et al., 2005). To capture this full complexity, model simulations would become rather computationally expensive and slow in performance. However, missing this complexity also substantially limits the current understanding of the budget of secondary pollutants, e.g., O_3 and aerosols. The challenges are twofold: 1) to understand and include the chemical degradation pathways, and 2) to also represent all other influencing processes (e.g. deposition, multiphase chemistry) in already complex global/regional models.

A chemical mechanism that stands out for size and detailed oxidation of many important VOCs is the Mainz Organic Mechanism (MOM, Sander et al., 2019). MOM represents the chemistry of alkanes, alkenes, terpenes (isoprene and monoterpenes) and monocyclic aromatics. The mechanism has been employed to study the impact of isoprene OH−recycling above pristine tropical forests (Taraborrelli et al., 2012), oxidation of monoterpenes as a source of HO_2 (Hens et al., 2014; Mallik et al., 2018) and the influence of aromatics on tropospheric ozone (Taraborrelli et al., 2021). Furthermore, MOM has been used with extensions in order to simulate product yields of β-caryophyllene oxidation (van Eijck et al., 2013), the oxidation of alkyl amines and formamide as source of isocyanic acid HNCO (Rosanka et al., 2020), the atmospheric losses of stabilised Criegee intermediates (Vereecken et al., 2017), and the most recent OH-recycling mechanisms in isoprene oxidation (Novelli et al., 2020). Yet, a full evaluation of the VOC distribution predicted by MOM in a global numerical model has not been published.

Furthermore, a more detailed chemical mechanism, which reduces the number of lumped species of larger VOCs, allows an explicit coupling of the VOC chemistry with an interactive aerosol phase partitioning and an organic compound ageing, without losing the chemical identity of the organic compounds. Previous studies (e.g. Farina et al. (2010); Tsimpidi et al. (2016)), which treat the organic aerosol with the help of a volatility basis set (VBS) (Donahue et al., 2011), usually use lumped species to represent tracers with similar volatility and age structure (e.g. O:C ratio, e.g. Ng et al. (2010)) therefore without any chemical identity or detailed degradation scheme. Instead, explicit chemistry schemes allow a representation of Secondary Organic Aerosols formation from VOCs without the use of lumped species and experimentally derived parameters (e.g., reaction rates, aerosol yields). These tuning parameters can increase model uncertainties and result in large differences between Atmospheric Chemistry models. In addition, empirical chemical schemes are not mass conserving (e.g., for carbon) and the higher-generation reaction products are lumped or ignored, even if, for instance, they play a pivotal role for OH recycling and ozone chemistry (Taraborrelli et al., 2012), or are a major component of atmospheric brown carbon (Laskin et al., 2015). In general, explicit identities of model species are essential for making further progress in quantifying the atmospheric budget of Secondary Organic Aerosols. By relying on high-quality (experimental and theoretical) data of the physico-chemical properties of precursors and intermediates, an ever more realistic modelling of removal, ageing and formation pathways would be possible.

In this study we present a simulation and an evaluation of the ECHAM/MESSy Atmospheric Chemistry (EMAC) general circulation model (Jöckel et al., 2010, 2016) with a complex organic chemical mechanism (MOM, Sander et al., 2019), accounting not only for the gas phase chemistry, but also for the losses via uptake/condensation into aerosols (via the ORACLE submodel) and cloud droplets (via the SCAV submodel). As the EMAC model has been largely evaluated in the past and for most of the components there were no significant changes, we focus on the evaluation of organic tracers and aerosols. Most importantly, general properties of the aerosols (such as aerosol optical depth (AOD) and particulate concentration below 2.5 $\mu g \, m^{-3}$) will be discussed, as these could be strongly affected. Furthermore, changes to the global hydroxyl radical distribution influenced by the new chemistry adopted in this study are discussed.

A comparison for VOCs with the MIM chemical mechanism developed by Pöschl et al. (2000) that has been evaluated by Pozzer et al. (2007) and used previously (Jöckel et al., 2006, 2016) is not shown here as in such mechanism (i) most of organics are either lumped, e.g. methyl vinyl ketone (MVK) and methancrolein (MACR), or missing, e.g. aromatics and monoterpenes; (ii) primary species common to MIM and MOM would be influenced only by the different sinks (mainly OH), and a detailed description of OH budget is presented here; (iii) the model bias with respect to secondary species, e.g. oxygenated VOCs, has been linked to a mis-representation or lack thereof processes like in-cloud chemistry (Rosanka et al., 2021b; Franco et al., 2021). Therefore any comparison of VOC simulations between MOM and MIM would not give any additional information on the model-observation discrepancy and aid any future model improvement.

The model set-up is presented in Sect. 2, followed by the description of the observational dataset used for the evaluation (Sect. 3), which is then presented for different tracers and aerosol components. This model evaluation is the basis for future studies on complex organic chemistry with EMAC.

2 Model configuration

EMAC is a numerical chemistry and climate simulation system that includes submodels describing tropospheric and middle-atmosphere processes and their interaction with oceans, land, and human influences (Jöckel et al., 2016). It uses the second version of the Modular Earth Submodel System (MESSy2) to link multi-institutional computer codes. The core atmospheric model is the 5th generation European Centre Hamburg general circulation model (ECHAM5 Roeckner et al., 2006). For the present study, we applied EMAC (ECHAM5 version 5.3.02, MESSy version 2.54.0) in the T63L31-resolution, i.e. with a spherical triangular truncation of T63 (corresponding to a quadratic Gaussian grid of approx. $1.8°$ by $1.8°$ in latitude and longitude) and 31 vertical hybrid pressure levels up to 10 hPa, with roughly 22 levels in the troposphere. The dynamics have been weakly nudged (Jeuken et al., 1996; Jöckel et al., 2006) towards the ERA-interim data (Berrisford et al., 2011) of the European Centre for Medium-Range Weather Forecasts (ECMWF) to reproduce the actual day-to-day meteorology in the troposphere. In this study we simulated two years (2009-2010), with the first year used as spin-up time.

The anthropogenic emissions are based on the Emissions Database for Global Atmospheric Research (EDGARv4.3.2 Crippa et al., 2018), vertically distributed following Pozzer et al. (2009), and has been compared to other global emission databases by Crippa et al. (2018). These prescribed emissions are included in the model via the OFFEMIS submodel (Kerkweg et al.,

80 2006b). The biogenic emissions of non-methane volatile organic compounds (NMVOC) are calculated on-line using the Model of Emissions of Gases and Aerosol from Nature (MEGANv2.04, Guenther et al., 2006, 2012). Lightning NO_x production is based on the parametrization of Grewe et al. (2001), while the algorithm of Yienger (1995) is used for soil NO_x emissions, as described in detail in Jöckel et al. (2016).

Biomass burning emissions are calculated daily online based on dry matter burned from observations and fire type (Kaiser

85 et al., 2012). The emission factors for different tracers and fire types are taken from Andreae (2019) and Akagi et al. (2011). The ONEMIS submodel (Kerkweg et al., 2006b) calculates natural emission fluxes of sea-salt (Guelle et al., 2001) and of dust (Klingmüller et al., 2018; Astitha et al., 2012). Oceanic emissions and deposition are calculated online with the AIRSEA submodel (Pozzer et al., 2006; Fischer et al., 2012; Lana et al., 2011) for DMS, CH_3COCH_3, CH_3OH, C_5H_8, HCN, and CH_3CN (a net sink for CH_3OH, HCN, and CH_3CN, a net source for the others). For C_2–C_3 alkanes and alkenes, the oceanic

90 offline emissions from Inness et al. (2012) have been adopted.

In Table 1 the total emissions are listed for all primary species emitted in the model.

Table 1: Emissions of primary emitted species for the year 2010 used in this study. The units are in $\mathrm{Tg(species)\,yr^{-1}}$ with the exception of NO_x, in $\mathrm{Tg(N)\,yr^{-1}}$

Tracer	extended name	Anthropogenic	Natural/Biogenic	Biomass Burning
BC	Black Carbon	4.34		1.84
OC	Organic Carbon	11.05		15.53
SO2	Sulfur Dioxide	99.35		1.95
NOx	nitrogen oxides	34.50	6.09	3.98
CO	carbon monoxide	537.16	106.84	289.51
NH3	ammonia	57.67		4.07
C2H6	ethane	9.00	1.32	2.91
C3H8	propane	10.50	1.46	0.52
HCN	hydrogen cyanide		2.13	
CH3CN	acetonitrile			1.03
NC4H10	n-butane	9.90		0.12
IC4H10	i-butane	4.20		0.04
MEK	methyl ethyl ketone	1.00	0.18	0.45
CH3CHO	acetaldehyde	2.00	15.35	2.80
CH3COCH3	acetone	1.10	35.84	1.29
CH3CO2H	acetic acid	6.52	3.45	13.20
CH3OH	methanol	9.71	105.54	6.32
HCOOH	formic acid	3.56	3.45	2.32

CH3COCO2H	pyruvic Acid		0.36	
HCHO	methanal,formaldehyde	4.50	5.17	4.15
C2H4	ethene	5.40	24.55	3.55
C3H6	propene	4.26	15.76	3.01
C2H2	acetylene	5.40		0.23
BUT1ENE	1-butene	1.46	6.23	0.07
TBUT2ENE	1,2-dimethylethylene	1.46		0.05
CBUT2ENE	2-butene	1.46		0.20
MEPROPENE	methylpropene	1.46		0.20
BENZENE	benzene	5.82		1.42
TOLUENE	toluene	7.80	0.35	0.83
LXYL	xylenes	7.24		0.28
LTMB	trimethylbenzenes	0.95		0.06
PHENOL	phenol	1.70		2.02
STYRENE	styrene	1.87		0.16
EBENZ	ethylbenzene	1.91		0.56
LHAROM	other aromatics	3.22		2.86
C5H8	isoprene		463.89	
APINENE	α-pinene		33.18	
BPINENE	β-pinene		18.71	
CARENE	3-carene		6.94	
SABINENE	sabinene		7.13	
CAMPHENE	camphene		3.20	
MBO	methyl butenol		1.36	
LTERP	lumped other terpenes		31.86	
LALK4	lumped pentanes	15.1		
LALK5	lumped higher alkanes	21.2		
OLE2	lumped higher alkenes	8.20		
DMS	Dimethyl sulfide		57.96	

Dry deposition and sedimentation are estimated by DDEP and SEDI submodel (Kerkweg et al., 2006a), while wet deposition is simulated by the SCAV submodel (Tost et al., 2006). The dissolution of species in the liquid phase mechanism was augmented by including liquid-gas equilibrium for all additional organics present in the mechanism with a Henry's law constant (solubility) above $10^3 \, \mathrm{mol \, L^{-1} \, atm^{-1}}$. For less soluble species, wet scavenging is not expected to be important (Crutzen and Lawrence, 2000). The Henry's law constants of most oxygenated VOCs of atmospheric relevance are unknown and estimation methods

95

still quite uncertain (Wang et al., 2017). As the hydroxyl (and hydroperoxyl) group affects the solubility in water the most, the Henry's law constants of polyols from the compilation by Sander (2015) are taken as proxies.

In the chemistry submodel MECCA, we used the Mainz Organic Mechanism (MOM, Sander et al., 2019), with roughly 600 species and 1600 reactions. It originates from a reduced isoprene oxidation mechanism (Taraborrelli et al., 2009), which has been updated with recent kinetic data and expanded with efficient mechanisms of OH-recycling under low-NO conditions (Taraborrelli et al., 2012; Nölscher et al., 2014). The oxidation mechanism for α-pinene and β-pinene is based on the MCM (E. Jenkin et al., 2000) with modifications according to the theoretical work of L. Vereecken (Vereecken et al., 2007; Capouet et al., 2008; Nguyen et al., 2009; Vereecken and Peeters, 2012). The degradation of monocyclic aromatics follows the MCM (Jenkin et al., 2003; Bloss et al., 2005) but with some modifications for the chemistry of phenols (Cabrera-Perez et al., 2016). The complete mechanism used in this study is part of the electronic supplement.

Aerosol microphysics and gas/aerosol partitioning are calculated by the Global Modal-aerosol eXtension (GMXe) aerosol module (described by Pringle et al., 2010a, b). GMXe simulates the distribution of aerosol within interacting lognormal modes (in a similar approach to that of Vignati et al., 2004; Mann et al., 2010). The lognormal modes span four size categories (nucleation (< 6 nm radius), Aitken (6–60 nm), accumulation (60–600 nm), and coarse (>700 nm)), and are divided into hydrophilic (4) and a hydrophobic (3) modes. The GMXe model has been extensively evaluated (Pozzer et al., 2012a, b; Tost and Pringle, 2012; Karydis et al., 2016).

Organic Aerosol (OA) formation is simulated by the submodel ORACLE (Tsimpidi et al., 2014, , v.1.0), where logarithmically spaced saturation concentration bins are used to describe the organic aerosol components based on their volatility. For the formation of primary (POA) and secondary (SOA) organic aerosol from the emissions and photochemical oxidation of semivolatile and intermediate volatility organic compounds the setup of Tsimpidi et al. (2016) is used. However, the SOA formation from the oxidation of the volatile organic compounds (VOC) in ORACLE has been modified to accommodate the photochemical production of components explicitly calculated by the MOM chemical mechanism. An earlier version of MOM has been compared against chamber measurements (Nölscher et al., 2014) and improved by Novelli et al. (2020), while ORACLE was derived empirically from chamber experiments (Donahue et al., 2011) and has been evaluated against observations from a field campaign by Janssen et al. (2017). Nevertheless, the MOM + ORACLE combination still has to be fully evaluated.

The effective saturation concentration of all the species present in the MECCA submodel is calculated based on their elemental composition (number of carbon, oxygen, nitrogen, and sulfur atoms), following the molecular corridor approach (Li et al., 2016) and the study by Donahue et al. (2011). In Figure 1, the volatility versus the molar mass is shown for all tracers present in the model, ranging from high volatility – low molar mass to low volatility – high molar mass. These calculations result in 199 tracers which, under atmospheric conditions, can partition to the aerosol phase forming SOA (i.e., with a volatility lower than 3.2×10^3 μg m^{-3}), while the other 396 tracers are considered too volatile for any condensation on aerosol particles. Additionally, the enthalpy of vaporization for the same condensing species has been estimated based on the study by Epstein et al. (2010). In addition to the 199 tracers, 11 additional "lumped species" for different oxidation levels of pentanes, higher alkanes, higher alkenes and terpenes have been added. Then, ORACLE calculates the partitioning of these organic species between the gas and particle phases by assuming a bulk equilibrium, and by further assuming that all organic compounds form
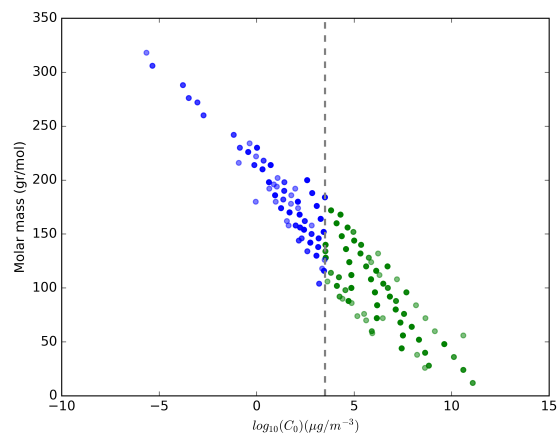
Figure 1. Saturation mass concentrations at 298 K (Li et al., 2016) versus molar mass of organic tracers in EMAC. The blue dots represent those included in ORACLE, i.e., organic tracers which, under atmospheric conditions, are allowed to condense explicitly on aerosols, the green dots represent those organic tracers always in the gas phase. The dashed line represents the maximum volatility considered in ORACLE (i.e. $3.2 \times 10^3 \, \mu g \, m^{-3}$) for the VOC oxidation products.

a pseudo-ideal solution. The aerosol size distribution is determined by distributing the change in aerosol mass after the bulk equilibrium into each size mode using a weighting factor (Tsimpidi et al., 2014).

The aerosol optical properties are calculated with the submodel AEROPT (Dietmüller et al., 2016), which is based on the scheme by Lauer et al. (2007) and makes use of predefined lognormal modes (i.e., the mode width σ and the mode mean radius have to be taken into account). Lookup tables with the extinction coefficient, the single scattering albedo, and the asymmetry factor for the shortwave, and extinction coefficient for the longwave part of the spectrum are pre-calculated with the help of Mie theory-based explicit radiative transfer calculations (see Pozzer et al., 2012a; Dietmüller et al., 2016). The aerosol compounds explicitly considered for their refractve indices are organic carbon, black carbon, dust, sea salt, water-soluble compounds (WASO, i.e. all other water soluble inorganic ions, e.g.: NH_4^+, SO_4^{2-}, HSO_4^-, NO_3^-), and aerosol water (H_2O).

3 Observational data

3.1 Aircraft measurements

Due to the high complexity of the MOM mechanism, we do not expect the model to be capable of representing polluted episodic conditions. Additionally, investigations of these conditions should be accompanied with detailed process studies, as done in previous studies with this mechanism (e.g. Lelieveld et al. (2018); Tadic et al. (2021)). Instead we want to demonstrate its ability to reproduce background conditions in a climatological sense. For this reason three different aircraft databases were

chosen, that are based on profiles of several flights and seasons, being over background regions, and providing an extensive set of observed trace gases.

3.1.1 NASA ATom campaign

150 We used observational data from the NASA Atmospheric Tomography Mission (ATom). The ATom campaign took place from July 2016 to May 2018 and included measurements in four different seasons (6 flights each). During the flights with the NASA DC-8 aircraft numerous profiles were recorded (see Figure 2), which makes the dataset perfect for the evaluation of atmospheric model simulations. The data used in this evaluation was taken from the "Merged Atmospheric Chemistry, Trace Gases, and Aerosols, Version 2 dataset" (Wofsy et al., 2021) and is based on various instruments: UC-Irvine Whole Air

155 Sampler (WAS; Barletta et al., 2019), Trace Organic Gas Analyzer (TOGA; Apel et al., 2021), California Institute of Technology Chemical Ionization Mass Spectrometer (CIT-CIMS; Allen et al., 2019), NOAA Chemical Ionization Mass Spectrometer (NOAACIMS; Veres et al., 2021), Georgia Tech Ionization Mass Spectrometer (GTCIMS; Huey et al., 2019), NOAA Nitrogen Oxides and Ozone Instrument (NOyO3; Ryerson et al., 2019) and NOAA Picarro G2401 spectrometer (NOAA-Picarro; McKain and Sweeney, 2021). The ATom observations were subdivided into data for different regions for this study (Fig-

160 ure 2; namely Northwest Pacific, Southwest Pacific, East Pacific, Southern Ocean, South Atlantic, North Atlantic, and North Canada/Alaska/Greenland) based on expected homogeneous properties of organic compounds in those regions. A climatological comparison between the simulated year (2010) and the data from the ATom campaign (2016-2018) will be performed in order to further evaluate, if the MOM mechanism is able to reproduce remote conditions. For that purpose we divided the altitude range into 12 bins (linearly between 0.5 and 12.5 km) and defined a maximum of 336 (7 regions $\times$ 4 seasons $\times$ 12

165 altitude bins) points of interest (POI). For each POI we compared the mean value of all observations in the specific region, altitude bin and season to the mean value of all accordingly simulated values in 2010 in the range of $\pm$ 1 day around the flights conducted in that region.

3.1.2 Emmons database

Additionally, we used the database of aircraft measurements of trace gases produced by Emmons et al. (2000). It is based on

170 observations from numerous aircraft campaigns that took place during the period 1990–2001 to create observational-based climatologies of chemical species relevant to tropospheric chemistry. Although these measurements cover only limited time periods and regions, they provide valuable information about the vertical distribution of the analysed trace gases. Note that the field campaigns used in this evaluation have been extended, also including observations after the year 2000, such as those from the TOPSE and TRACE-P campaigns.

175 ### 3.1.3 Heald database

The aircraft evaluation is completed by aircraft measurements for organic aerosols presented by Heald et al. (2011). This dataset includes organic aerosol measurements from 17 aircraft campaigns during the period 2001–2009. Here, similar to Emmons
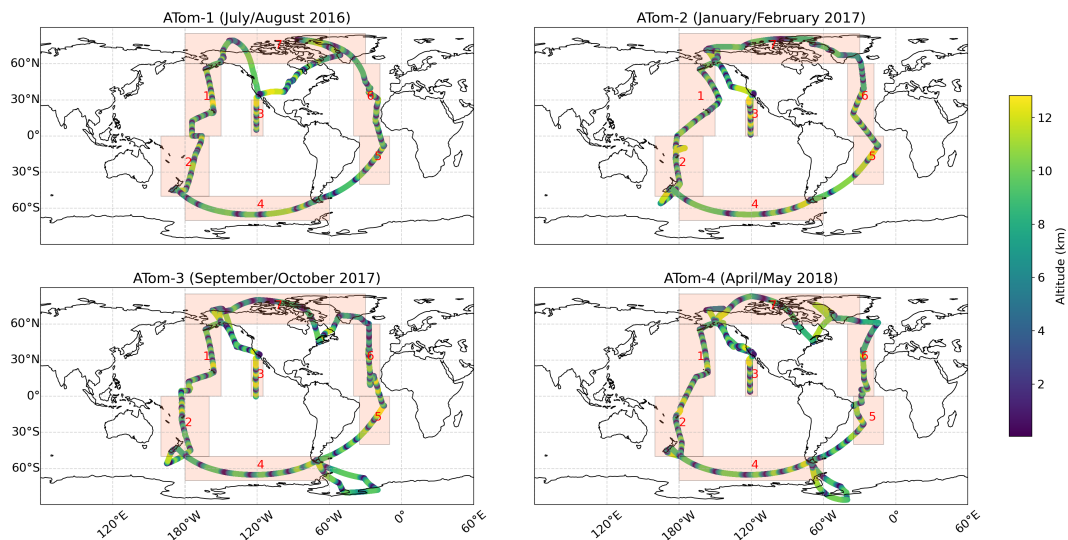
Figure 2. Flight paths of the 4 ATom campaigns. The respective altitude is colored and the paths are sub-divided into 7 different remote regions, namely Northwest Pacific (1), Southwest Pacific (2), East Pacific (3), Southern Ocean (4), South Atlantic (5), North Atlantic (6), and North Canada/Alaska/Greenland (7).

et al. (2000), we consider the aircraft campaigns representative for the period and the regions, i.e., as an observational-based climatology. Therefore, we compared these data with the model results for the year 2010, yielding an improved evaluation of

180   the vertical distribution of the organic aerosols in the troposphere.

3.2 Station measurements

3.2.1 NOAA-INSTAAR

Data from the National Oceanic and Atmospheric Administration (NOAA) Institute of Arctic and Alpine Research (INSTAAR) Global Monitoring program were also used in this study. The network consists of 44 background stations from the NOAA

185   Global Greenhouse Gases Reference Network (GGGRN) (Pollmann et al., 2008), where pairs of whole air samples are collected weekly and shipped to a central laboratory for analyses. For this study, we considered measurements of ethane, propane, iso- and n-butane from this network.

3.2.2 EPA

The Clean Air Markets Division of the U.S. Environmental Protection Agency (EPA) operates the Clean Air Status and Trends

190   Network (CASTNET), with a total of 97 stations. Here, we include weekly filter pack data from 81 stations for SO_4^{2-}, NO_3^-,

NH_4^+, Na^+, Mg^{2+}, Ca^{2+}, K^+ and Cl^- for the year 2010. The data can be downloaded at www.epa.gov/castnet, last access on December 10, 2020.

3.2.3 IMPROVE

In order to evaluate the simulated regional background OA concentrations, we use monthly averaged $PM_{2.5}$ OA measurements during the year 2010 from the Interagency Monitoring of Protected Visual Environments (IMPROVE) program (http://views.cira.colostate.edu/fed, last access on September 21, 2021). IMPROVE is a cooperative measurement effort in the United States designed to characterize current visibility and aerosol conditions in scenic areas (primarily National Parks and Forests). This network includes 198 monitoring sites that are representative of the regional haze conditions over North America. IMPROVE collocated samplers collect 24 hour samples every three days.

3.2.4 EMEP

The co-operative programme for monitoring and evaluation of the long-range transmission of air pollutants in Europe (EMEP) is a scientifically-based and policy-driven programme under the Convention on Long-range Transboundary Air Pollution for international co-operation to solve transboundary air pollution problems. We use data from 42 stations, although the number of stations providing sufficient data for a certain species ranges from 22 to 42 (see Table 6). As Teflon filters are used predominantly, depending on the respective station, the concentrations of particulate nitrate can be systematically underestimated (Ames and Malm, 2001). The data were obtained from the EBAS database (http://ebas.nilu.no/, last access on September 21, 2021) and stations not providing full coverage of monthly mean values for the year 2010 were excluded from the analysis.

3.2.5 EANET

The Acid Deposition Monitoring Network in East Asia (EANET) regularly monitors acid deposition as from January 2001. Thirteen countries participate currently in this effort, submitting data from a total of 54 sites. We use monthly averaged aerosol concentrations from 15 to 25 stations for the year 2010, with the data obtained from the Network Center for EANET, at https://monitoring.eanet.asia/document/public/index, last access on September 21, 2021. It is worth mentioning that EANET does not include OA observations. The simulated $PM_{2.5}$ OA over East Asia is evaluated against collected short-term measurement data as summarized by Jo et al. (2013).

3.3 Remote sensing observations

3.3.1 MOPITT

The MOPITT (Measurement of Pollution in the Troposphere) is a sensor onboard the NASA's Terra satellite. We use the MOPO3JM version 8 product of MOPITT which provides monthly mean gridded column integrated CO, vertical profiles of CO mixing ratios at ten regularly spaced pressure levels from the surface up to 100 hPa as well as the corresponding averaging kernels (Deeter et al., 2019). The MOPO3JM product is based on the joint near-infrared (NIR) and thermal-infrared (TIR)

retrievals of CO. We apply the MOPITT averaging kernels on the EMAC CO profiles according to equation 1 to ensure the same level of smoothing as that in the MOPO3JM product.

$$x_{rtv} = Ax_{true} + (I - A)x_a \tag{1}$$

Here, x_{true} is the EMAC profile, x_a is the a priori profile, A is the averaging kernel matrix and I represents an identity matrix.

3.3.2 MODIS

The MODerate resolution Imaging Spectroradiometer (MODIS) sensor is also located on the Terra satellite. Here, AOD550 data (i.e., Aerosol Optical Depth at 550 nm) from the MODIS Level 3 (Col. 6.11) gridded product are used at a spatial resolution of $1° \times 1°$. The data are available through the Atmosphere Archive & Distribution System (LAADS) (https://ladsweb.modaps.eosdis.nasa.gov/ , last access on September 21, 2021). Here the Deep Blue algorithm (Hsu et al., 2004) was used for the aerosol AOD.

3.3.3 IASI

Global observations of a suite of VOCs are retrieved from the thermal infrared measurements of the nadir-viewing IASI (Infrared Atmospheric Sounding Interferometer) instruments (Clerbaux et al., 2009). The VOC dataset exploited here consists of total column densities of methanol, acetone, formic and acetic acids, and PAN, retrieved near-globally on a daily basis from the IASI/Metop–A observations with the aid of the ANNI (Artificial Neural Network for IASI) v3 retrieval framework. This neural network-based retrieval approach does not rely on a priori information of the total column densities and, hence, the products can be used directly for unbiased comparisons with model data (see Franco et al., 2018; Whitburn et al., 2016). The satellite products are filtered for measurements affected by clouds and poor retrieval performance. The uncertainties on the individual retrieved column densities can be large, but are considerably reduced by averaging numerous observations in space and time, as done in this study by comparing annual averages on the model grid. A full description of the ANNI framework, the characterization of the VOC products, and comparisons of the satellite data with independent measurements can be found in Franco et al. (2018, 2019, 2020); Mahieu et al. (2021), and references therein. These studies, thanks to comparisons with ground-based column density measurements of VOCs, as well as with column densities derived from aircraft profiles, indicate no large systematic biases of the IASI data and no dependence on the latitude, although an underestimation (locally up to 30%) of the highest column densities over tropical source regions (e.g., the Amazon Basin) has been identified for all the IASI VOC products, except for PAN. The accuracy of the IASI measurements is therefore sufficient to provide a global evaluation of the EMAC performance, considering the large uncertainties that still affect the emissions and atmospheric modelling of the VOCs. For both, IASI and the model, daily gridded averages were constructed at the spatial resolution of the model grid. To have similar temporal coverage over the year between model and satellite observations, the EMAC daily averages were masked when the corresponding IASA data were missing for the same day and location.

3.3.4 AERONET

The AOD observations have been obtained from the global AErosol RObotic NETwork (AERONET Holben et al., 1998; Dubovik et al., 2000). The cloud-screened quality-assured Level 2 AOD data used in this study were obtained from the website http://aeronet.gsfc.nasa.gov/cgi-bin/combined_data_access_new (last access on September 21, 2021) including AOD daily averages.

3.4 Pseudo observations

Global annual averages of fine particulate matter with an aerodynamic diameter below 2.5 μm ($PM_{2.5}$) have been obtained from Hammer et al. (2020). In this dataset, a combination of satellite observed AOD, numerical model, and ground-based $PM_{2.5}$ measurements were used to estimate $PM_{2.5}$ on a global scale at high resolution.

4 Results

In Table 2 the evaluation of organic tracers using observations from the ATom campaign is presented, while Table 3 shows the comparison of the model results with the aircraft campaign data from Emmons et al. (2000) for selected tracers. There are no measurements of acetic acid (CH_3COOH) from the ATom campaign and the observations of Ethene (C_2H_4) and Propene (C_3H_6) are very limited. Thus, they will not be considered for discussion. In the Emmons database, there are no observations of i-Butane (iC_4H_{10}) and n-Butane (nC_4H_{10}).

CO, C_2H_6 and O_3 are very well represented, as for both observations, more than 85% of the simulated values are within a factor of 2 compared to the observations for these species (PF2). Other species, such as PAN show insufficient agreement with both observation sets, while again other species do not show a consistent behaviour in both comparisons. For some species (such as the alkene C_3H_6 in the Emmons database), a general clear underestimation is seen in the Emmons database, cohering with former results (Pozzer et al., 2006). An interesting feature can be observed for methyl hydroperoxide (CH_3OOH) and formaldehyde (HCHO). Both species are strongly underestimated by the simulation compared to the ATom observations (see Table 2; $\overline{MM/OM}$ of 0.47 and 0.61, respectively), while they are highly correlated with the observations (≈ 0.9). Thus, the vertical shape is very well reproduced, but the sources or the sinks seem to be systematically underestimated or overestimated, respectively. This feature is depicted in Figure 3. The evaluation results for selected species will be analysed in more detail in the following.

4.1 CO

Figure 4 shows the seasonal (MAM: March, April, May; JJA: June, July, August; SON: September, October, November; DJF: December, January and February) mean modified EMAC and MOPITT CO vertical column densities (VCD). Here, we term it as "modified" EMAC VCDs because MOPITT averaging kernels are applied on the simulated CO profiles to account for the

Species (Instrument)	N.points	MM	MSTD	OM	OSTD	$\overline{MM/OM}$	PF2	RMSE	CORR
CO (NOAA-Picarro)	332	76.86	18.98	81.22	23.99	0.98	100.0	10.56	0.82
C_2H_4 (WAS)	143	7.63	9.33	17.65	27.79	0.64	32.2	12.61	0.26
C_2H_6 (WAS)	334	369.47	191.54	550.41	375.48	0.79	86.5	195.09	0.87
C_3H_6 (WAS)	30	0.74	0.82	7.77	7.33	0.11	0.0	7.03	0.54
C_3H_8 (WAS)	330	48.38	65.63	83.64	130.04	0.97	61.5	44.92	0.87
CH_3COCH_3 (TOGA)	331	417.38	127.29	370.67	259.18	2.37	74.3	163.93	0.6
CH_3OH (TOGA)	333	372.0	186.19	601.5	393.94	1.02	64.0	292.98	0.5
CH_3OOH (CIT-CIMS)	306	161.03	143.64	419.17	412.65	0.47	33.0	259.92	0.89
HCHO (TOGA)	321	102.31	82.41	156.88	106.11	0.63	73.2	55.81	0.92
HCOOH (NOAACIMS)	168	39.44	21.43	188.59	359.94	0.61	35.7	155.87	0.3
HNO_3 (CIT-CIMS)	334	207.64	350.83	121.83	259.36	2.98	42.5	127.17	0.69
H_2O_2 (CIT-CIMS)	334	470.86	444.63	363.72	397.68	2.11	68.9	153.47	0.87
PAN (GTCIMS)	241	30.71	34.7	75.43	51.33	0.54	36.5	50.13	0.38
O_3 (NOyO3)	334	88.26	113.49	66.01	80.95	1.37	92.5	26.5	0.89
iC_4H_{10} (TOGA)	319	6.88	13.72	9.71	18.63	0.83	52.7	4.94	0.89
nC_4H_{10} (TOGA)	316	15.79	31.81	17.14	33.62	1.17	58.5	8.41	0.89

Table 2. Summary of simulated and observed mixing ratios of different tracers from the ATom campaign (Wofsy et al., 2021). N.points is the number of points used for the statistical estimation. The arithmetic mean of the model simulated mixing ratios (MM), the observed mixing ratios (OM), and the corresponding standard deviations (MSTD, OSTD) in $\mathrm{pmol/mol}$ are listed in the subsequent columns. For CO and O_3 the units are in $\mathrm{nmol/mol}$. PF2 denotes the percentage of simulated points within a factor of 2 with respect to the observations, and RMSE represents the root mean square error between simulated and observed points. CORR is the Pearson correlation coefficient.

sensitivity of MOPITT. To highlight the difference in spatial patterns of EMAC and MOPITT, we also show the absolute bias in the bottom panel.

We note that the spatial patterns are in good agreement between simulation and observations. In particular, the elevated CO background in the outflow regions (over oceans) in the northern hemisphere is well represented during boreal winter (DJF) and spring (MAM). The outflow region around south America in SON is also simulated well. Over land, a good agreement is found for Europe, central and Eastern United States, northern Africa, Australia, Russia, and the Indian subcontinent with a mean bias within $\pm 1 \times 10^{18}$ molecules cm^{-2}. During the biomass burning seasons (JJA in central Africa, north and north-east China and SON in south America), we observe an overestimation of $\sim 30\%$ by EMAC. By comparing EMAC's total CO column densities to IASI CO satellite retrievals, Rosanka et al. (2021a) found that EMAC underestimates CO in Indonesia in SON 2015. In 2015, a particularly strong El Niño led to severe peatland fires, which resulted in large CO emissions. Rosanka et al. (2021a) attribute the underestimation to a too low biomass burning emission factor for peatland used by EMAC. Here, we do

Species	N.points	MM	MSTD	OM	OSTD	$\overline{MM/OM}$	PF2	RMSE
CO	457	90.41	32.63	94.86	72.11	1.03	99.3	63.991
C_2H_4	454	25.16	139.23	45.93	175.49	1.06	45.2	110.05
C_2H_6	473	539.19	320.22	826.09	544.14	0.70	88.8	409.24
C_3H_6	332	6.25	63.13	13.70	53.09	0.40	6.9	32.64
C_3H_8	472	94.96	123.26	164.99	225.57	0.89	59.7	149.02
CH_3COCH_3	246	520.61	274.71	608.50	310.84	0.92	87.4	291.65
CH_3OH	37	595.76	369.59	913.86	373.06	0.66	78.4	426.52
CH_3OOH	366	210.71	190.79	376.80	321.19	0.66	52.7	251.34
HCHO	213	198.08	377.76	192.24	299.65	1.44	64.3	235.36
HCOOH	53	32.67	7.05	58.92	43.55	0.87	64.1	49.41
CH_3COOH	53	13.50	7.08	51.08	28.31	0.34	20.7	46.51
HNO_3	416	151.33	188.49	162.15	285.72	1.25	59.9	237.42
H_2O_2	411	634.08	611.96	745.48	875.21	1.09	80.0	516.44
PAN	395	62.46	71.30	162.60	186.81	0.61	40.0	185.79
O_3	506	68.23	76.00	51.06	26.10	1.31	92.6	62.54

Table 3. Same as Table 2, but for the comparison of our simulation results to the dataset of Emmons et al. (2000)

.

not find any underestimation of CO in Indonesia in SON (see Fig. 4), since the year 2010 was a year with little biomass burning emissions in Indonesia (van der Werf et al., 2017). Following their analysis, the recent biomass burning emission factor estimate by Andreae (2019) suggests that EMAC underestimates the CO emission factor by about 10 % in Central South America and Africa. It must however be stressed that the uncertainties on biomass burning emissions are substantial, depending on regions

295 and species (Carter et al., 2020). In contrast, in South America the overprediction of EMAC's CO column densities can be partially attributed to EMAC's tendency to overestimate biogenic emissions of CO precursors in this region (see Rosanka et al., 2021b, a), as also shown in Sect. 4.2.3 and Sect. 4.2.4.

Figure 5 shows the 2010 annual mean measured and simulated surface CO mixing ratio at the WDCGG stations sorted according to their latitude coordinates. The relative bias at all stations is also shown on a global map in the inset of Figure

300 5. Similar latitudinal gradients are seen for the measurements and simulations with high values around the mid-latitudes of the northern hemisphere. The measured and simulated CO agree within 1σ annual variability for 106 out of 113 stations for which data were available for the year 2010. The bias between model and simulation was found to be less than 20 % of the observations for 96 stations.
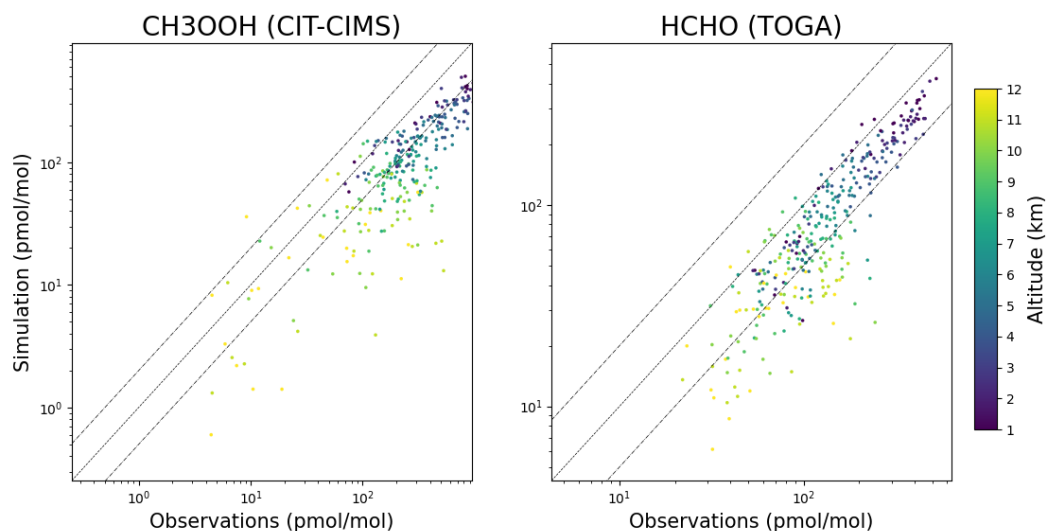
Figure 3. Scattered simulated values of CH_3OOH and HCHO against the observations of the ATom measurements. The different colors represent the altitude. Both species are generally underestimated by our simulations, but at the same time highly correlated between simulation and observations.
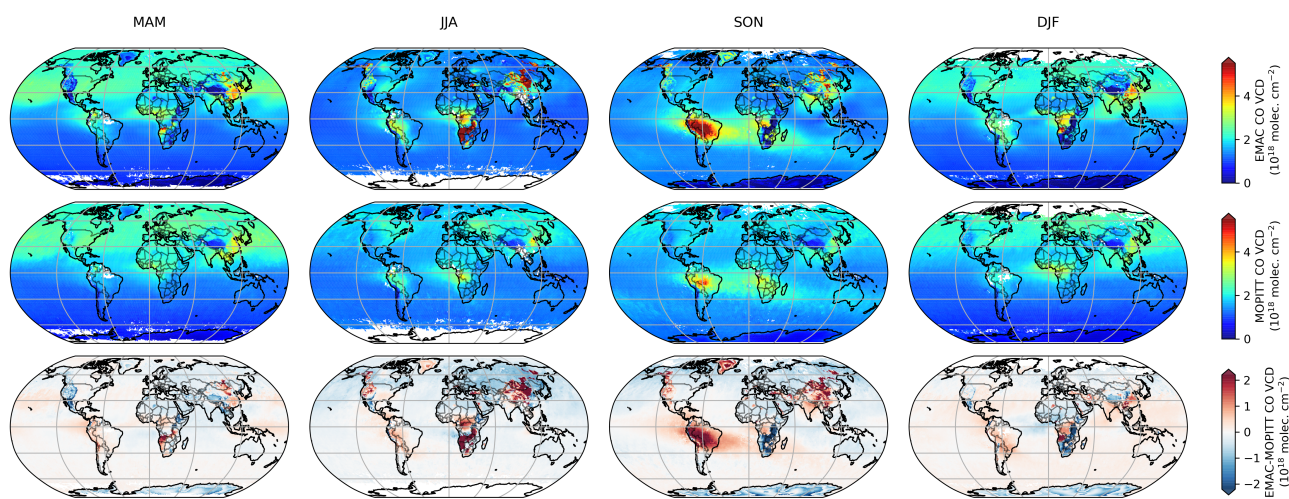
Figure 4. Global seasonal mean maps of CO vertical column densities (VCD) for the year 2010 for EMAC (top), MOPITT (middle), and bias (EMAC - MOPITT), (bottom).
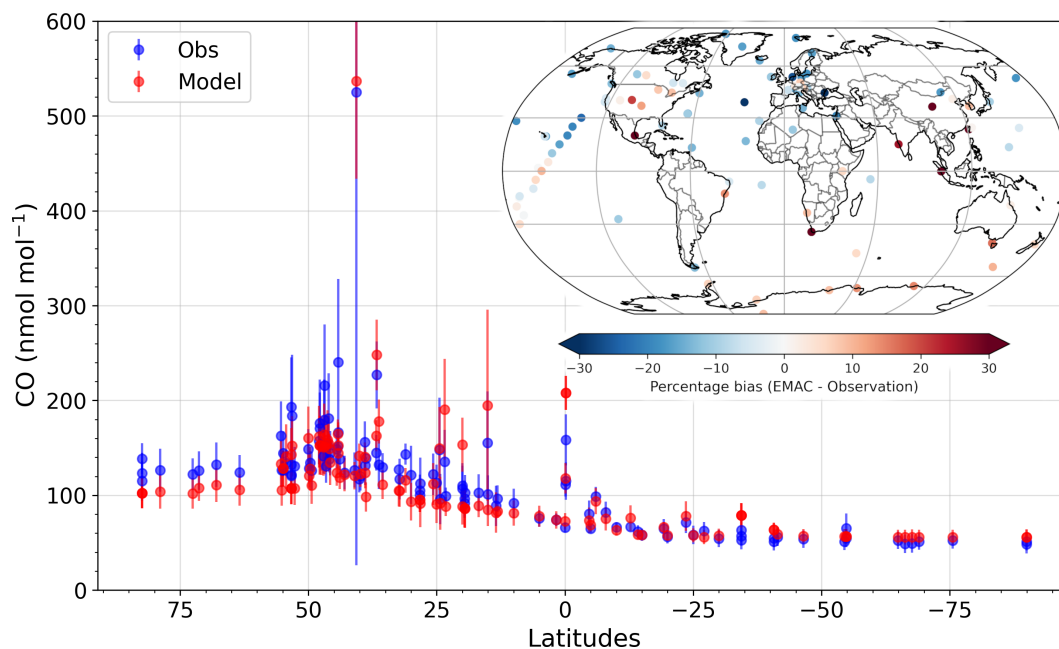
Figure 5. Latitudinal gradient of the annual mean (2010) of the measured and simulated surface CO mixing ratio at the WDCGG measurement stations. The error bars show the 1σ standard deviation of the annual mean (based on daily mean output). The map in the inset shows the annual bias between the simulation and measurements at the locations of the WDCGG stations.

4.2 Volatile organic compounds

4.2.1 C_2-C_4 Alkanes

Alkanes are VOC ubiquitously present in the atmosphere, mainly emitted from anthropogenic activities. In Figure 6 the scatter plots of model results and in-situ observations from the NOAA/INSTAR database are presented. The statistic for each plot is summarized in Table 4. The model seems to reproduce satisfactorily the mixing ratios of the C_2-C_4 alkanes with more than 98, 91, 84 and 79 % of the simulated values lying within a factor of two to the observations for C_2H_6, C_3H_8, $i-C_4H_{10}$ and $n-C_4H_{10}$, respectively. Furthermore, the average ratios show that a slight overestimation is present for i-butane and n-butane, whereas the model underestimates the mixing ratios of ethane and propane. This is confirmed by the comparison with the Emmons et al. (2000) database (Table 3), which shows that both, ethane and propane, are underestimated by the model, also with respect to the vertical profile (column $\overline{MM/OM}$). The comparison with ATom observations (Table 2) shows an underestimation of ethane and propane (albeit smaller) as well. However, for i-butane we see a slight underestimation in the evaluation using ATom observations in contrast to the NOAA/INSTAR database.

Figure 6 shows also a noticeable underestimation of the mixing ratios in the region between 30° N and 0° N, for propane and the butanes. This is clearly due to the underestimation of the oceanic emissions, as these stations (i.e., at Mahe Island, Sey-
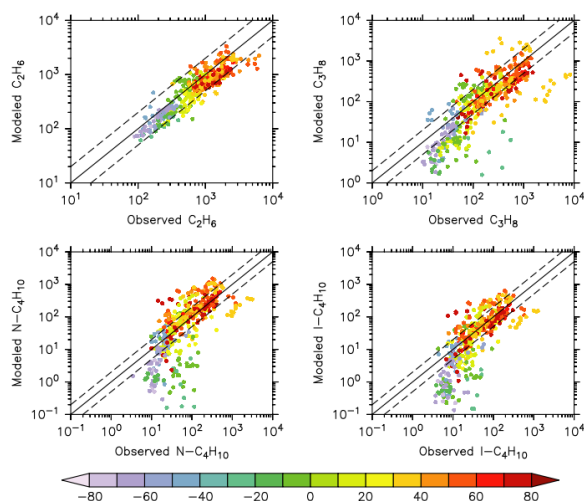
Figure 6. Scatter plot of measured and simulated surface alkanes mixing ratios at the NOAA/INSTAAR measurement stations for the year 2010. The units are in $\mathrm{pmol\,mol^{-1}}$. The color code denotes the latitude of the stations.

chelles (SEY), The American Samoa Observatory (SMO), Ascension Island, UK (ASC), and Easter Iland, Chile (EIC)) are all strongly influenced by oceanic emissions. It must be pointed out that for $i-C_4H_{10}$ and $n-C_4H_{10}$, no oceanic emissions where included in the simulation, but that these are necessary for a correct representation of butanes, as already shown previously (Pozzer et al., 2010). However, the underestimation in this region is not present in the comparison to the ATom observations.

Species	N.points	MM	MSTD	OM	OSTD	$\overline{\mathrm{MM/OM}}$	PF2	RMSE
C_2H_6	450	742.54	551.02	1038.32	845.09	0.77	98.4	621.54
C_3H_8	447	262.87	417.25	393.13	745.48	0.91	91.5	755.93
$i-C_4H_{10}$	436	70.60	97.44	73.73	126.46	1.23	84.8	124.23
$n-C_4H_{10}$	423	160.49	231.75	146.89	293.97	1.46	79.6	307.80

Table 4. Summary of simulated and observed mixing ratios of different tracers in the NOAA/INSTAAR database (station observations). The columns are as in Table 3

.

4.2.2 C$_2$-C$_3$ Alkenes

Differently from alkanes, the alkenes are mostly emitted by the biosphere. The comparison to the ATom campaign can only be based on a very limited number of observations, and thus will not be subject of this discussion. As shown in Table 3 in the comparisons with the Emmons et al. (2000) database, the numerical simulation of alkenes diverges more from the observations than the simulated alkanes do. Both, C_2H_4 and C_3H_6, are underestimated compared to the observations (see model mean against observed mean in Tab. 3). Nevertheless, while C_2H_4 is overall reasonably reproduced (average of the ratios equal to 1.06, see Table 3), for C_3H_6 a strong underestimation is present (average of the ratios equal to 0.4, see Table 3). This is shown in Fig. 7, where examples of the vertical distribution of C_2H_4 are shown. The issues in simulating C_3H_6 have been already pointed out by Pozzer et al. (2006), where similar results were obtained with large underestimation of this tracer. As alkenes are mostly removed by reaction with OH, there are strong indications that these reactions are too fast, in addition, a substantial lack of emissions could be present, for instance from natural sources as suggested by (Li et al., 2021).

4.2.3 CH$_3$OH

CH_3OH is the most abundant oxygenated VOC in the Earth's atmosphere (Singh et al., 2001), primarily emitted by the terrestrial vegetation (Jacob et al., 2005). Other sources include biomass burning, the oceans and secondary formation in the troposphere (e.g., Millet et al., 2008; Stavrakou et al., 2011). The annual global distribution of CH_3OH total colum densities obtained from the IASI measurements and EMAC of the year 2010 as well as their differences are presented in Fig. 8. Over land, the satellite and model spatial distributions of CH_3OH are relatively consistent, with the main source regions observed within the tropics (mainly over the Amazon Basin and central Africa), in Southeast Asia, and at Northern Hemisphere mid- and high latitudes. However, important differences in magnitude exist. Over the tropical forests, EMAC indeed simulates annual CH_3OH colum densities up to two times larger than those retrieved from the IASI observations (3.0–3.5×10^{16} molecules cm^{-2}). This can be partly ascribed to the high temperature bias that exists in the model over these areas (Hagemann and Stacke, 2015), which induces an excess of biogenic VOC emissions from the MEGAN submodel due to its high temperature sensitivity (Guenther et al., 2006). This is confirmed by a comparison of the simulated isoprene mixing ratios in the Amazon rainforest with observations from the AMAZE-08 campaign (Martin et al., 2016) and from the ATTO tower (Yáñez Serrano et al., 2015). In comparison to the AMAZE-08 campaign, the simulated isoprene measurements are overestimated by more than a factor of 3 (6.1 ± 1.2 nmol/mol simulated and 1.9 ± 1.4 nmol/mol observed), while the overestimation factor for the ATTO tower is on average approximately 1.6, being higher in February/March and lower in October/November.

Furthermore, dry deposition of methanol in tropical rainforests is likely under-represented by the Wesely (1989) approach used here (Karl et al., 2004). The potential contribution of an additional non-stomatal pathway favourable under humid conditions (Müller et al., 2018) has been shown by Emmerichs et al. (2021) for a less soluble species. On the other hand, EMAC underestimates the CH_3OH column densities at mid- and high latitudes of the Northern Hemisphere, indicating that biogenic and/or biomass burning VOC emissions are too low during summertime in these regions. Southeast US is the region in North America where most of the simulated CH_3OH enhancement exists, driven by substantial biogenic emissions in summertime,
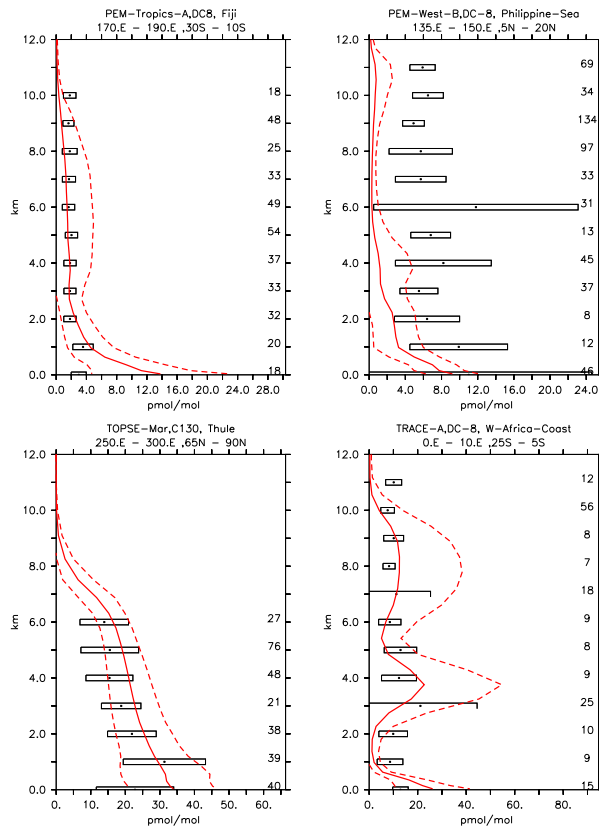
Figure 7. Vertical profiles of C_2H_4 in $\mathrm{pmol\,mol^{-1}}$ for some selected campaigns from Emmons et al. (2000). Asterisks and boxes represent the average and the standard deviation (w.r.t. space and time) of the measurements in the region, respectively. The simulated average is indicated by the red line and the corresponding simulated standard deviation w.r.t. time and space by the dashed lines. On the right hand side, the number of measurements is listed.

355   while larger column densities are measured by IASI during the same season further northwards in the boreal regions. Over the oceans, EMAC underestimates the observed CH_3OH column densities by $\sim 5 \times 10^{15}\ \mathrm{molecules\,cm^{-2}}$, which might result from an insufficient transport from the continental source regions and/or from missing secondary source(s) (see e.g., Bates et al., 2021; Müller et al., 2016). This is confirmed by the comparison of model results with the aircraft observations of the ATom campaign and the Emmons et al. (2000) database, where the methanol model mean is considerably lower than the ob-
360   served one. This is most prominent over Pacific regions in the Northern Hemisphere at lower altitudes as depicted in Figure 9. However, with respect to the vertical profile CH_3OH is not generally underestimated in comparison with the ATom campaign, as it is rather overestimated at higher altitudes and for lower absolute values.
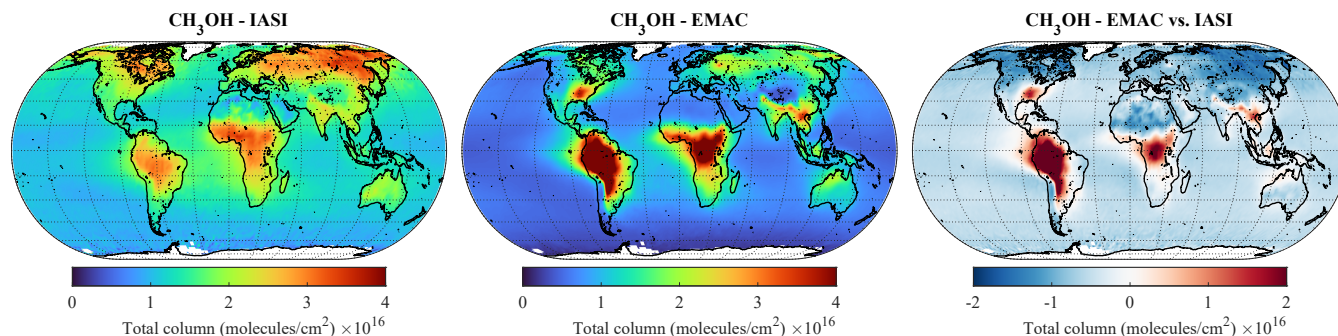
Figure 8. Annually averaged CH_3OH total column densities (in $molecules\,cm^{-2}$) from IASI satellite observations (left), simulated by EMAC (middle), and the EMAC–to–IASI column density differences (right), for the year 2010.
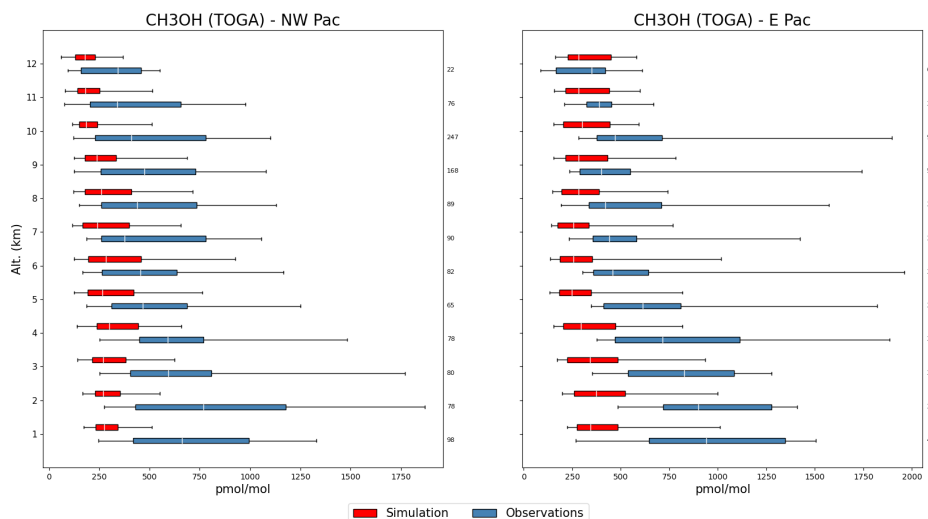
Figure 9. Vertical profiles of CH_3OH of model simulations and ATom observations over the Pacific region (region 1 in Fig. 2) on the Northern Hemisphere, represented by box–whisker plots for altitude bins. The white line marks the median, the box corresponds to lower and upper quartiles, the whiskers represent the 5–95 percentile. The numbers on the right indicate the number of points of interests (POI, avereaged values for region, flight and altitude) considered for each altitude bin.

4.2.4 CH_3COCH_3

Acetone is the one of the most abundant oxygenated VOCs in the Earth's atmosphere after CH_3OH (Singh et al., 2001). Its
365   sources include the terrestrial vegetation, the oxidation of hydrocarbon precursors of biogenic and anthropogenic origin, the oceans and biomass burning (e.g., Jacob et al., 2002; Pozzer et al., 2010; Fischer et al., 2012). The acetone column densities
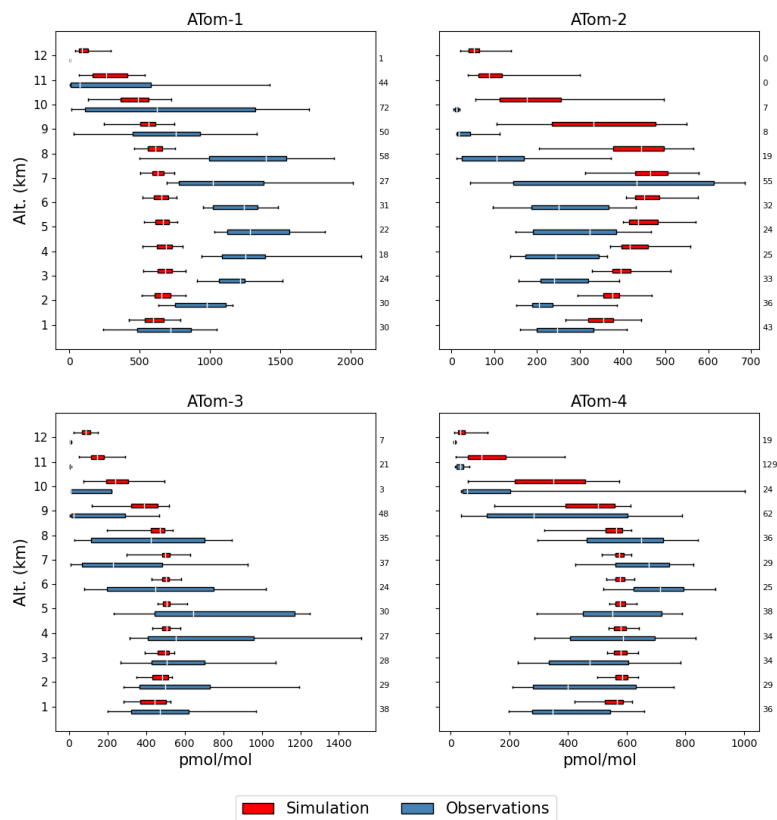
Figure 10. As Fig.9 but for CH_3COCH_3 and for the region over Canada, Alaska and Greenland (region 7 in Fig. 2) for the different ATom campaigns / seasons.

obtained from the EMAC simulation and the IASI observations exhibit major discrepancies in terms of global distribution (Figure 11). The satellite instrument detects the largest acetone column densities (up to 2×10^{16} molecules cm^{-2}) at mid- and high latitudes of the boreal hemisphere, ascribed to important emissions of biogenic precursors during summertime (Franco

370 et al., 2019), but a moderate burden at low latitudes and over the tropical forests. It is worth noting that this pattern is in agreement with the global acetone measurements obtained with the ACE–FTS satellite limb sounder (Dufour et al., 2016). Conversely, EMAC simulates strong hotspots of acetone within the tropics, especially over South America and Africa, with annually averaged column densities larger than 2×10^{16} molecules cm^{-2}, but underestimates the acetone abundance by up to a factor of 2 in the Northern Hemisphere. Such a mismatch between satellite and model distributions points to major deficiencies

375 in the current emission inventories of acetone and its precursors. For example, the extremely large acetone column densities simulated by EMAC over the Persian Gulf and the Indo Gangetic Plain can be attributed to the highly elevated emissions
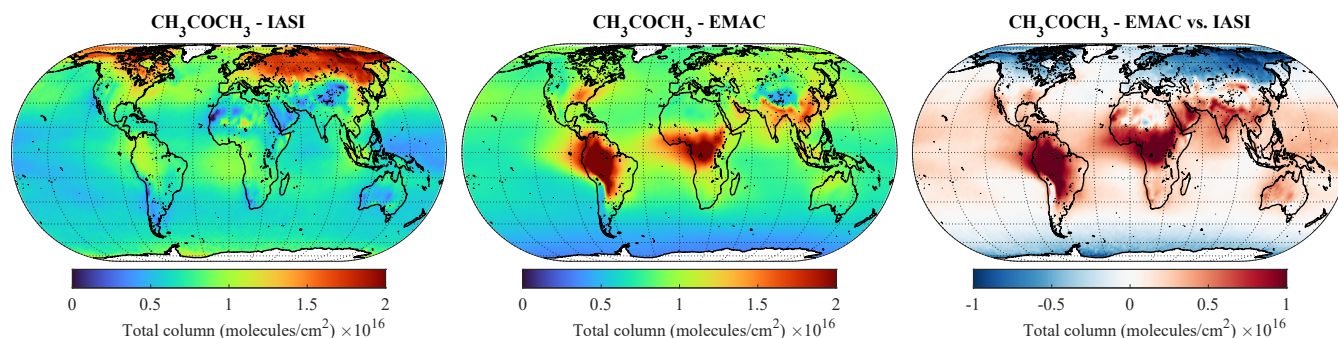
Figure 11. Same as Fig. 8, but for CH_3COCH_3.

of propane – an important precursor of acetone – in these regions. In vegetated regions, an underestimation of acetone dry deposition, accounting globally for 20 % of the total loss (Khan et al., 2015), likely contributes to the mismatch. According to measurements, significant amounts of acetone are removed during night through non-stomatal uptake (Karl et al., 2004; Müller et al., 2018). However, over remote areas and the oceans, the simulated acetone abundance is consistent with the IASI measurements, with vertical column densities in the range of $0.5–1.0 \times 10^{16}$ molecules cm^{-2}. The model, nevertheless, simulates a slight overestimation over the oceans at low latitudes compared to IASI, especially in the outflows of the tropical hotspots.

Compared to the ATom observations the model overestimates the mixing ratios, especially at high altitudes leading to a large value of $\overline{MM/OM}$, while the simulatedd and observed mean are of a comparable magnitude. However, there are still 74.3% of the simulated values within a factor of 2 of the observations (see Table 2). Figure 10 depicts the vertical column densities of observations and simulations over the northern part of North America and Greenland, a region where CH_3COCH_3 is largely underestimated by the model in comparison to IASI. In Northern Hemisphere summer (July/August; ATom-1) this strong underestimation can be observed as well for the ATom observations. However, for other seasons, this is not the case. Overall, simulation results show only a small underestimation for this region. Compared to the Emmons et al. (2000) database, the model results present a much better agreement, with only a somewhat small bias (see Tab. 3). This apparent agreement with the observations is due to the uneven distribution of the field campaign present in the observational dataset (see Emmons et al. (2000), Fig.1 and Huijnen et al. (2019), Fig.1). In fact, most of the campaigns in which acetone was measured took place over the ocean, where the model is correct or slightly overestimating the total column densities observed by IASI. In contrast, only few campaigns in the Northern Hemisphere are present in the dataset (such as ABLE-3B, and POLINAT-2) for which the model strongly underestimates the observed values. As a result of the sparsity of these observations, Table 3 presents a quite fair agreement between model and aircraft observations, an agreement which is, however, not corroborated by the more spatially complete comparison with the IASI total column densities.
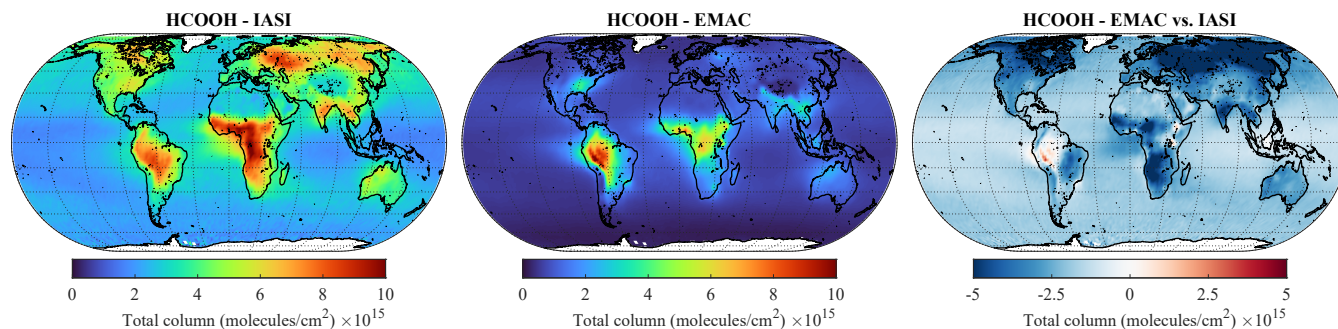
Figure 12. Same as Fig. 8, but for HCOOH.

4.2.5 HCOOH

Formic acid is the dominant organic acid in the troposphere and a product of the degradation of a large suite of VOC precursors, but its observed abundance is generally severely underestimated by state-of-the-art global models (e.g., Millet et al., 2015; Paulot et al., 2011; Stavrakou et al., 2012). Similarly, in our simulation the EMAC model largely underestimates the HCOOH total column densities derived from the IASI observations by up to a factor of 4, in particular in remote environments (see Fig. 12). Although the two main tropical source regions identified by IASI – the Amazon Basin and central Africa – are reproduced by EMAC, the magnitude of the simulated HCOOH column densities are too low in comparison to the satellite measurements. It also has to be mentioned that the apparent agreement over Amazonia is possibly due to the high temperature bias in the region and the subsequent excess of simulated isoprene emissions during the dry season. Over the other source regions (e.g., Southeast Asia and Southeast US), the model underestimation is more pronounced, in particular in the Northern Hemisphere. The large enhancement of HCOOH column densities observed with IASI over western Russia ($\sim 8 \times 10^{15}$ molecules cm^{-2}), attributed to the August 2010 wildfires, is not reproduced by EMAC ($<2 \times 10^{15}$ molecules cm^{-2}) and suggests that the biomass burning emissions of VOCs are underestimated.

The general underestimation of simulated versus observational data is also confirmed by the comparison with aircraft observations. Especially at low altitudes and for high absolute values the model strongly underestimates the observations by the ATom campaign (see Table 2, the observed mean is higher by more than a factor of 4 compared to the model mean). In general, there is very low agreement between simulated values and ATom observations as only around 35% of the simulated values are within a factor of 2 of the observations and the Pearson correlation coefficient is only 0.3. Although the underestimation of the model results to the Emmons et al. (2000) database is less apparent it must be noted that only a limited number of merged data (53, see Table 3) is available for the comparison with aircraft observations. It must be stressed that Franco et al. (2021) showed the importance of in-cloud chemistry for this tracer, which is missing in this study. The lack of adequate in-cloud chemistry would therefore explain the almost ubiquitous underestimation of this tracer.
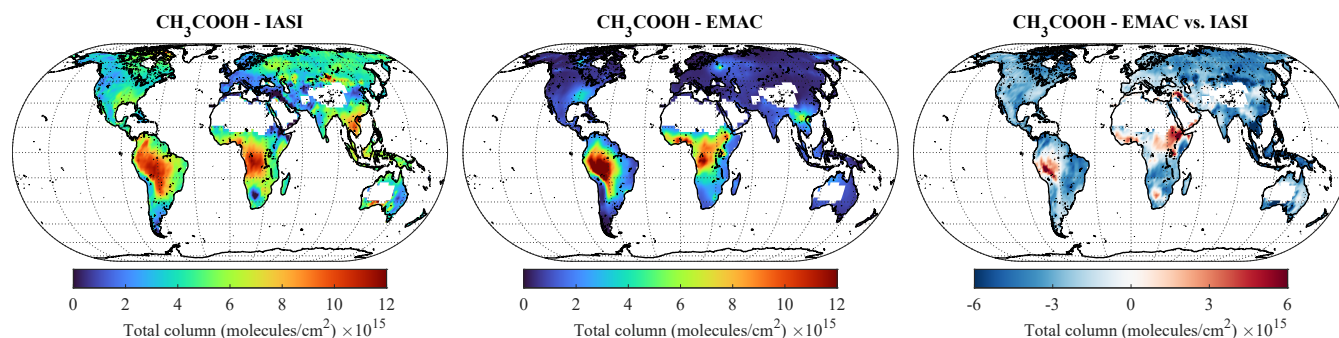
Figure 13. Same as Fig. 8, but for CH_3COOH. In this figure area above the ocean were excluded.

4.2.6 CH_3COOH

Acetic acid is the second most abundant carboxylic acid in the troposphere and, based on the IASI retrievals, presents a spatial pattern, regional seasonality, and vertical abundance, which resemble those of HCOOH (Franco et al., 2020). Like the latter, CH_3COOH is produced from the oxidation of various tropospheric precursors, but has emission factors from biomass burning that are 3 to 10 times larger than those of HCOOH (Akagi et al., 2011; Andreae, 2019). CH_3COOH is more difficult to detect in the infrared IASI spectra and its retrievals are subject to larger uncertainties, in particular over the oceans (see Franco et al., 2020). Therefore, we limit here the comparison with EMAC to the continents, excluding measurements over desert areas that are altered by surface emissivity artefacts (Fig. 13). From the comparison, conclusions similar as for HCOOH can be drawn for CH_3COOH: the two main tropical source regions are relatively well reproduced by EMAC (with a better agreement over Africa in this case), whereas the observed CH_3COOH levels are underpredicted in the Northern Hemisphere by up to a factor of 4. The comparison with aircraft observations (see Table 3) confirms again this strong underestimation also over the ocean, as the only campaign in the dataset including CH_3COOH measurements is the PEM-Tropics-A, which was performed over the Pacific ocean.

These results confirm that the VOC emissions and oxidation pathways leading to the formation of CH_3COOH in the troposphere are still poorly understood and constrained (e.g., Khan et al., 2018; Paulot et al., 2011). For example, acetaldehyde – a major CH_3COOH precursor via its reaction with OH (Lei et al., 2018) – is well known to be largely underestimated by global models (Millet et al., 2010; Wang et al., 2019). On the other hand, the large model versus observations differences in Southeast Asia also point to missing emissions from biomass burning. Finally, in-cloud chemistry could be important in the CH_3COOH formation, analogously to formic acid (Franco et al., 2021), and this process could bring model results and observations to a closer agreement.
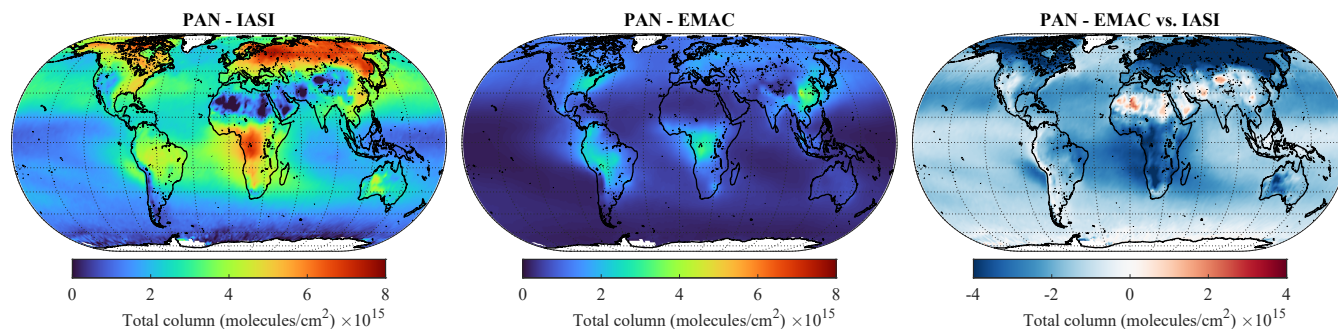
Figure 14. Same as Fig. 8, but for PAN.

4.2.7 PAN

Owing to its complex photochemical sources and its thermal instability, PAN (Peroxyacetylnitrate), the main tropospheric reservoir species of NO_x, is a very challenging tracer to simulate. The comparison with the IASI data reveals that the model reproduces correctly the main spatial patterns of PAN, with the source regions and main outflows over the oceans being correct. However, the model constantly underestimates the observed PAN column densities over the globe. The satellite column densities are indeed between two and four times the simulated ones, with the most pronounced negative bias observed at Northern Hemisphere mid- and high latitudes. The same conclusion can be drawn from the comparison with aircraft observations (Table 2 and 3), for which the model clearly underestimates the observed mixing ratios consistently using the database from Emmons et al. (2000) and the measurements of the ATom campaign. A closer inspection reveals that PAN is especially underestimated in the middle and upper-troposphere. The model–to–observations discrepancies can mostly be attributed to the unsatisfactory representation of different VOCs. For example, we have seen that the model results do not agree with observations for acetone, which is an important precursor of the peroxyacetyl radical in the free troposphere (Fischer et al., 2014). Furthermore, the strongest model's underestimation appears to be exactly where CH_3COCH_3 is at most underestimated, confirming that deficiencies of simulated precursor patterns are the main cause of the PAN biases. Additionally, sensitivity simulations suggested that the PAN formation in global models is more sensitive to the representation of VOCs (Fischer et al., 2014). Finally, an insufficient vertical transport of VOCs from the planetary boundary layer to the free troposphere in the model might also reduce the amount of PAN, because PAN is more stable at the lower temperatures of the free troposphere.

4.3 OH

The simulated distribution of the hydroxyl radical (OH) is in line with the findings by Lelieveld et al. (2016) (further denoted as L16), who earlier thoroughly analysed the MOM performance in EMAC with a setup featuring a simplified treatment of aerosol microphysics and gas/aerosol partitioning. The total OH turnover (composition of annual production and loss terms, shown in Fig. 15) of 234 $\mathrm{Tmol\,yr^{-1}}$ in 2010 is 7 % less than that found by L16 and is consistent with the addition of the

explicit treatment of secondary organic formation processes of aerosols and changes in trace gas emission fluxes. The OH production in the VOC- and ROOH-initiated reactions is 3 % lower in both, the free troposphere (FT), and the boundary layer (BL). This is compensated by the increased share of primary production (P, via the $O(^1D)+H_2O$ pathway), especially in the BL (4 % increase vs. 2 % in the FT). Regarding the partitioning of the OH sinks, however, no substantial changes can be noted (see Fig. 15, right panel). Together with the reduction of the secondary sources (S), the resulting OH recycling probability r_{OH} (defined as $1 - P/(S + P)$, see details in L16) establishes at 59 % and 62 % in the BL and FT, respectively. Being about 5 % lower than the estimate reckoned by L16, such high r_{OH} values signify still highly stable (buffered) OH concentrations and therefore a likewise stable tropospheric oxidative capacity obtained with this model set-up.
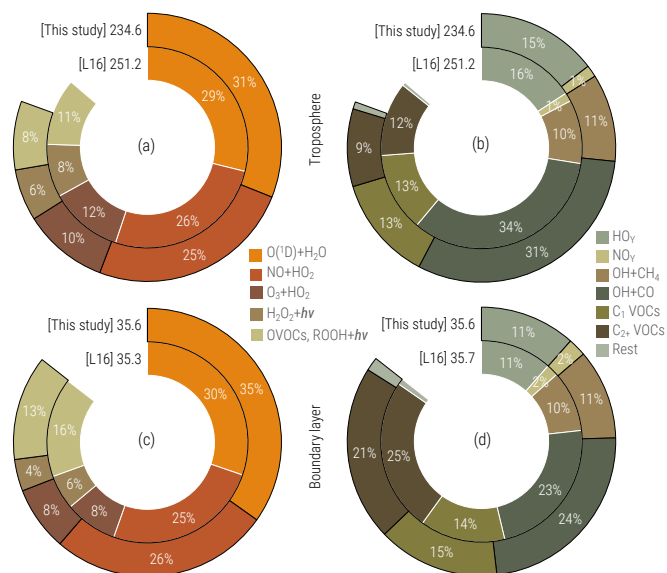
Figure 15. Simulated OH production (left) and sink (right) by category in the troposphere (top) and boundary layer (bottom) in this study and by Lelieveld et al. (2016) (denoted L16). Values are annual totals in $Tmol/yr$ for 2010. Percentages denote fractions attributed to particular categories (see L16 for for details).

The simulated annual air mass-weighted average OH concentrations are 12.1 (troposphere), 12.0 (FT) and 13.6 (BL) $10^5\,molecules\,cm^{-3}$ in the year 2010, which correspond to OH chemical removal lifetimes of 1.59, 1.78 and 0.53 s, respectively. The diagnosed tropospheric OH inter-hemispheric gradient (NH/SH ratio) is 1.17, lower than that estimated by L16 (1.20) due to the increased OH reactivity via VOC and SOA in the NH and at the lower end of the model estimates reviewed there. By not being in agreement with the measurement-based estimates suggesting hemispheric symmetry in tropospheric OH (Patra et al., 2014; Wolfe et al., 2019), the pronounced asymmetry in atmospheric models results from asymmetric OH production due to skewed distributions of O_3 and NO_x prevailing in the NH, and calls for further studies in this direction.

Overall, the simulated tropospheric OH distribution is comparable to that thoroughly analysed by L16 with a minor increase in reactivity of up to 5 % when calculated from the changes to the CH_4 and MCF (CH_3CCl_3) lifetimes against removal by OH

480 (τ_{OH}). The here estimated $\tau_{\mathrm{OH}}(\mathrm{CH_4})$ values are 8.4 and 4.4 years in the FT and BL, respectively; the tropospheric $\tau_{\mathrm{OH}}(\mathrm{MCF})$ value is obtained to be 4.9 years.

4.4 Aerosol Optical Depth

In order to evaluate the overall performance of the model in reproducing aerosol distribution, the AOD at 550 nm simulated by the model is compared to satellite based and station observations. Figure 16 shows the annual average AOD of the simulation
485 and of the observations (satellite). The distribution is remarkably similar, with the high AOD regions (Northern Africa and Soth Eastern Asia) being well simulated by the model. Open ocean AOD of $\simeq 0.2$ AOD units are reproduced by the model, with slightly underestimated AOD over the central Atlantic (possibly due to slightly underestimated dust outflow from the northern Africa region). To quantify the model capability to reproduce the AOD, in Figure 17, the model daily AODs are compared to the collocated (in space and time) observations from MODIS and the AERONET instruments (middle and bottom
490 row, respectively). For comparison, the same scatter plot has been produced comparing MODIS and AERONET directly (top row). The model has difficulties in reproducing the daily variability of AERONET AOD, with only 58 % of the simulated AOD within a factor of 2 to the observational data. Even the correlation is considerably low, with an R^2 equal to 0.33. Very similar results are obtained by comparing the model results to the satellite AOD observations, with again only 57 % of the simulated data within a factor of 2 to the observations. Once monthly averages are used for the inter-comparison, the statistics
495 remain almost unchanged with just a small improvement in the slope of the fitting curve (see Fig. 17, central column). Finally, using the annual averages for the intercomparison, the coefficients of determination R^2 almost double (0.633 and 0.567 for the comparison of the model with MODIS and AERONET data, respectively), while more than 80 % of the model results are within a factor of 2 to the observations (either satellite or in-situ). To put these results into context, the same analysis has been performed comparing the MODIS data and AERONET stations. Although the satellite observations outperform (slightly)
500 the model results compared to the AERONET measured AOD in the case of the daily and monthly averages, for the annual averages the model seems to perform equally well, with a similar coefficient of determination and a fraction of values within a factor of 2 to the observations. Due to the intrinsic characteristics of the model (such as its relative coarse resolution) it is not expected to have a good representation of the short term variability.

4.5 Fine particulate mater ($\mathrm{PM_{2.5}}$)

505 The comparison of model results for $\mathrm{PM_{2.5}}$ (i.e. fine particles with an aerodynamic diameter smaller than 2.5 μm) was performed against the dataset of Hammer et al. (2020). Although this dataset is not a pure observational dataset, it has a global coverage and has been constrained from in-situ measurements. The comparison is done for $\mathrm{PM_{2.5}}$ at 35 % relative humidity, i.e. dry fine particulate mass (in $\mathrm{\mu g\, m^{-3}}$). In Figure 18, the maps of the annual average of the model results and the pseudo-observation dataset are shown. Although the distribution patterns appear to be similar, the model underestimates the
510 fine particle concentration over northern India and eastern China, on the one hand, while the opposite happens over east Africa and the Middle East. On the other hand side, the model seems to reproduce $\mathrm{PM_{2.5}}$ quite accurately over both Europe and North
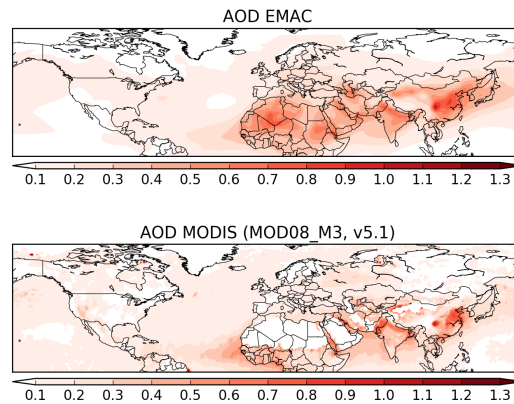
Figure 16. Global map of AOD from model results and the MODIS observations for the year 2010 (annual average).

America, and even the locally enhanced levels of $PM_{2.5}$ ($\sim 30\,\mu g\,m^{-3}$) in Canada from Boreal forest biomass burning are nicely reproduced by the model.

In Figure 19, the scatter plot of the two datasets is shown, while in Table 5 the statistics for the different regions presented in the figures are listed. Due to the large grid resolution difference, the pseudo-observations have been aggregated to the grid resolution of the model. As already noted from the global map, the model underestimate $PM_{2.5}$ over South Asia and East Asia by $\sim 40\,\%$ and $\sim 20\,\%$, respectively. Nevertheless, in both regions, more than $70\,\%$ of the model results are within a factor of 2 of the pseudo-observations. As shown by Pozzer et al. (2012a, 2017), and more recently by Miao et al. (2020), BC and OC are very important for the $PM_{2.5}$ budget in East and South Asia. As shown by Crippa et al. (2018) and Saikawa et al. (2017) the emissions of these tracers are associated with large uncertainties in these regions, which could strongly affect our results. The model agrees well, however, with data from Europe and North America, with more than $95\,\%$ of the model results within a factor of two. The overall comparison indicates that the model agrees well with the pseudo-observations, as the spatial-temporal averages of the two datasets are very close ($17.1\,\mu g\,m^{-3}$ for the model and $19.4\,\mu g\,m^{-3}$ for the pseudo-observations), with more than $70\,\%$ of the model simulated $PM_{2.5}$ within a factor of two of the pseudo-observed $PM_{2.5}$.

4.6 Aerosol Composition

For the evaluation of the simulated mass concentrations of sulfate, nitrate, ammonium, sodium and five species related to sea spray and organic aerosols, we use in-situ measurements from different monitoring networks, as described in Sect. 3.2. Co-located time series of simulated and observed quantities were obtained by bilinear interpolation of the gridded model data at ground level to the respective site location. The analysis is based on monthly mean concentrations, which are derived from daily (model data, EMEP observations) and weekly (EPA) data, with the exception of EANET, which directly provides monthly averages. Note that some monitoring stations are located relatively close to each other, such that the reported concentrations
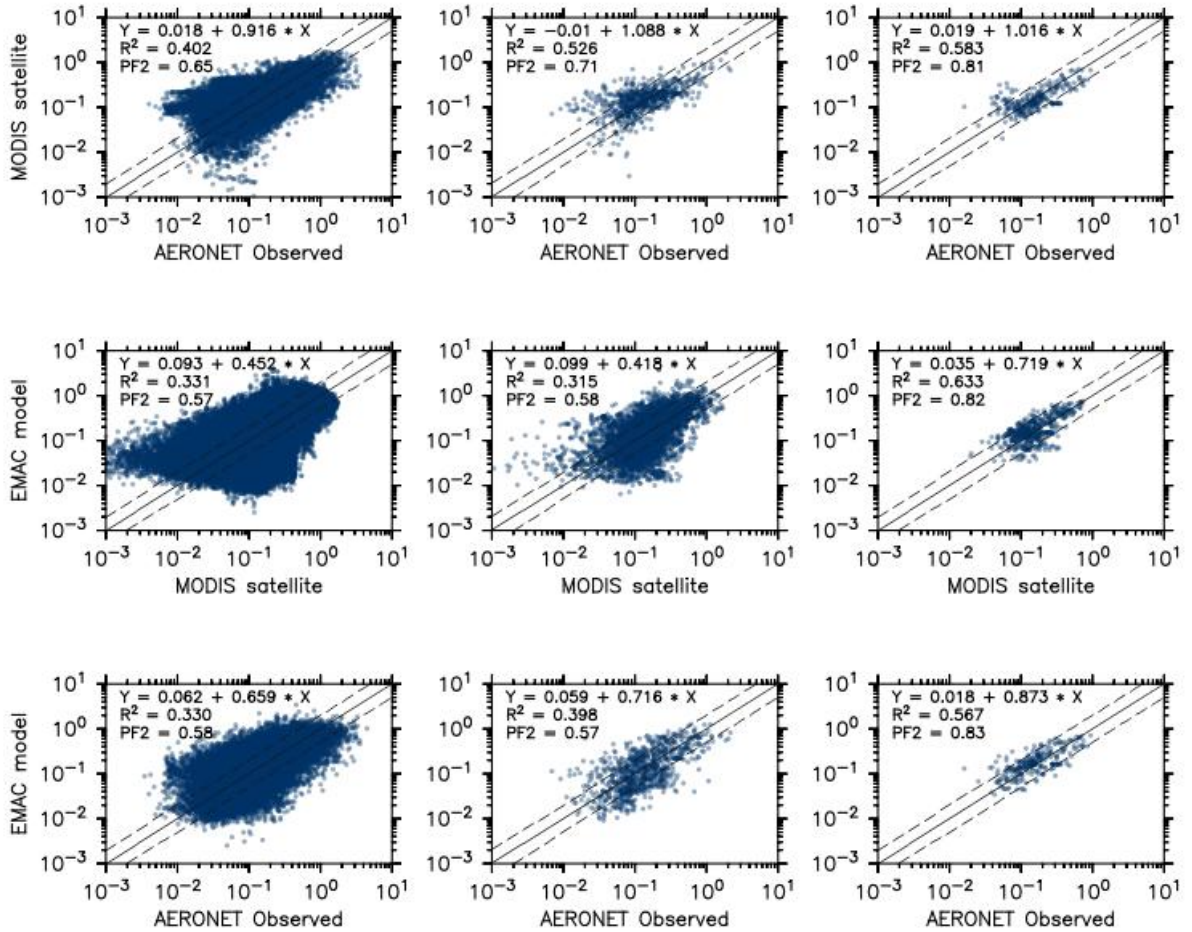
Figure 17. Scatter plots of AOD estimated by the EMAC model in this study versus the MODIS and the AERONET observations. Left, Middle and Right: scatter plots using daily, monthly and annual averages, respectively. Both, model and satellite based observations, were sampled at the AERONET locations. In each plot the coefficients of the linear fit, the coefficient of determination and the fraction of data within a factor of 2 are listed.

may not be independent from each other, which can lead to an overestimation of the degrees of freedom in the calculation of quantities such as the root mean square error.
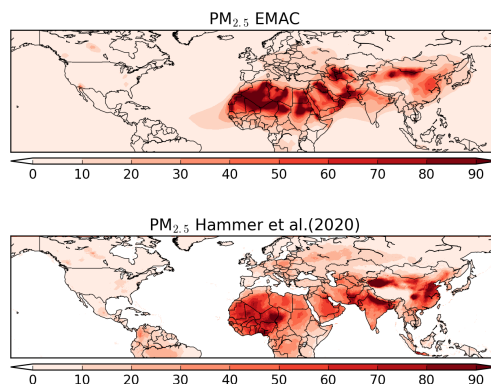
Figure 18. Global map of $PM_{2.5}$ from model results and the Hammer et al. (2020) dataset for the year 2010 (annual average) in $\mu gr/m^3$. The data from Hammer et al. (2020) does not contain values over the ocean.
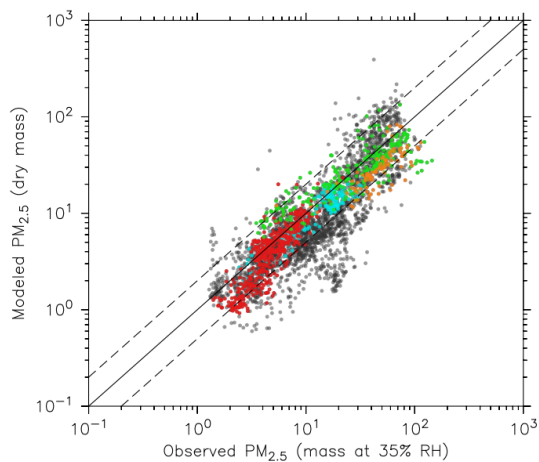
Figure 19. Scatter plots of $PM_{2.5}$ of model results versus data from Hammer et al. (2020) for the year 2010 (annual average) in $\mu g\,m^{-3}$. Light blue, red, green, and orange colors depict points located in Europe, North America, East Asia, and South Asia, respectively. Grey points indicate the remaining parts of the world.

4.6.1 Sulfate (SO_4^{2-})

535 Observed particulate sulfate concentrations are reproduced well by the model. The monthly mean concentration is matched closely for North America (EPA) and slightly underestimated for Europe (EMEP) and East Asia (EANET) (see Table 6).

Region	MM	OM	MM/OM	PF2
Europe	11.4	14.3	0.80	98.8
North America	4.8	5.2	0.92	95.2
South Asia	31.2	50.3	0.62	72.6
East Asia	31.2	37.1	0.84	82.1
World	18.4	19.4	0.94	71.4

Table 5. Summary for simulated and pseudo-observed, annually averaged $\overline{PM_{2.5}}$. MM and OM denote the arithmetic mean of the simulated and observed concentrations, respectively, in μgm^{-3}. PF2 is the percentage of simulated points within a factor of 2 with respect to the observations.

For EPA and EMEP data, more than 80% of the simulated monthly mean concentrations lie within a factor of two of the observations, and more than 70% for EANET. The standard deviation of observed monthly mean values is lower than the root mean square error (RMSE) for all monitoring networks, which is an indication for a good quality of the model results (Barna and Lamb, 2000). Also, RMSE is lower in the present study compared to a similar analysis by Pozzer et al. (2012a) in which, however, a longer time period of four years (2005-2008) was investigated. Pozzer et al. (2012a) also report a relatively large spread (observation standard deviation equal to 5.3 μgm^{-3}) of the measured sulfate concentrations in EANET, which is likely to be caused by a comparably low number of stations which cover a large region with strong spatial gradients.

The close overall agreement of average concentrations simulated by the model (MM) with the observations (OM) for EPA can partly be attributed to underestimated high concentrations in summer (composite of June, July and August, "JJA"), which are compensated by overestimated lower concentrations from autumn to spring (see Figure 20). Relative deviations are largest in winter and autumn, when observed concentrations are much lower than simulated concentrations. In Europe (EMEP), the highest concentrations are observed during the winter months, which is captured by the model.

The East-West gradient of observed annual mean concentrations in North America is represented well in the model, although the amplitude is underestimated by the model: lower observed values in the West are overestimated, while higher observed concentrations in the East are underestimated by the model (Figure 21). This feature also lead to a good agreement between observed and simulated mean concentrations in Table 6. The North-South gradient over Europe is also captured by the model. Despite the less dense spatial distribution of monitoring stations providing data for particulate sulfate, one can observe a correspondence between simulated and observed annual mean concentrations, especially over Japan. One outlier in Japan with a very low observed annual mean concentration is located at a relatively high altitude ("Happo", 1850 m), so that the comparison to model data on ground level may not be appropriate for this station. The same holds for two EMEP stations, namely Jungfraujoch (Switzerland) at 3578 m, and Chopok (Slovakia) at 2008 m, where annual mean concentrations are largely overestimated, possibly due to the coarse resolution of the model, which cannot reproduce correctly the orography (and hence the altitude) of these stations. We therefore compared SO_4^{2-} concentrations with observations from aircraft campaigns, as compiled by Heald et al. (2011). The results are presented in Fig.22. The simulated sulfate concentrations agree well with

Species	Network	$N_{station}$	MM	MSTD	OM	OSTD	$\overline{MM/OM}$	PF2	RMSE
SO_4^{2-}	EPA	81	1.92	0.99	1.88	1.20	1.35	84.3	0.93
SO_4^{2-}	EMEP	42	1.68	1.05	1.79	1.21	1.37	83.7	0.95
SO_4^{2-}	EANET	25	2.83	1.65	3.58	4.06	1.58	71.0	3.49
NO_3^-	EPA	81	1.89	1.97	0.77	1.07	4.29	36.9	1.88
NO_3^-	EMEP	22	3.34	2.89	1.93	2.15	3.75	55.3	2.97
NO_3^-	EANET	23	3.34	3.34	1.45	2.43	8.36	32.6	3.47
NH_4^+	EPA	81	1.09	0.89	0.73	0.53	1.84	64.8	0.77
NH_4^+	EMEP	27	1.31	1.17	0.92	0.86	1.69	62.0	0.92
NH_4^+	EANET	23	1.40	1.35	1.00	1.14	2.38	54.7	1.07
Na^+	EPA	81	0.16	0.22	0.16	0.36	2.19	61.1	0.23
Na^+	EMEP	24	0.57	0.43	0.60	0.73	2.03	53.1	0.57
Na^+	EANET	21	0.92	0.81	1.22	1.67	2.89	46.8	1.53
Mg^{2+}	EPA	81	0.05	0.06	0.05	0.05	2.06	42.7	0.06
Mg^{2+}	EMEP	22	0.17	0.13	0.07	0.09	4.65	32.6	0.16
Mg^{2+}	EANET	15	0.29	0.21	0.24	0.26	2.38	57.8	0.27
Ca^{2+}	EPA	81	0.06	0.12	0.26	0.27	0.60	16.2	0.37
Ca^{2+}	EMEP	28	0.14	0.25	0.15	0.25	1.60	51.5	0.24
Ca^{2+}	EANET	19	0.23	0.22	0.75	1.97	1.44	45.2	2.07
K^+	EPA	81	0.03	0.05	0.07	0.04	0.83	19.8	0.08
K^+	EMEP	25	0.09	0.13	0.08	0.07	1.42	60.0	0.14
K^+	EANET	20	0.12	0.09	0.26	0.34	0.98	47.1	0.37
Cl^-	EPA	81	0.35	0.65	0.14	0.51	5.92	24.7	0.53
Cl^-	EMEP	24	2.16	1.59	0.86	1.05	37.24	29.5	1.82
Cl^-	EANET	17	2.63	2.55	1.90	2.88	4.38	39.2	2.62
OA	IMPROVE	155	1.32	1.11	0.92	0.73	1.73	0.65	1.01
OA	EMEP	12	1.43	0.77	2.55	2.27	0.83	0.60	2.35
OA	EASIA	9	9.20	9.91	16.07	11.41	0.51	0.42	9.25

Table 6. Summary of simulated and observed monthly averaged aerosol concentrations for SO_4^{2-}, NO_3^-, NH_4^+, Na^+, Mg^{2+}, Ca^{2+}, K^+, Cl^- and organic aerosols (OA) and different observational networks (second column). $N_{station}$ is the number of stations providing data for the respective species and network; note that this is *not* the sample size for the shown statistics. The next columns provide the arithmetic mean of the simulated (MM) and observed concentrations (OM), and the respective standard deviations (MSTD, OSTD) in μgm^{-3}. PF2 denotes the percentage of simulated points within a factor of 2 with respect to the observations, and RMSE represents the root mean square error between simulated and observed points.

the aircraft observations in the free and lower troposphere, with an underestimation in a few cases (see Fig.22, ITCT-2K4, ADIENT or IMPEX campaigns), but always within the measurement standard deviations, confirming that the vertical profile of sulfate is generally well reproduced in the lower troposphere.
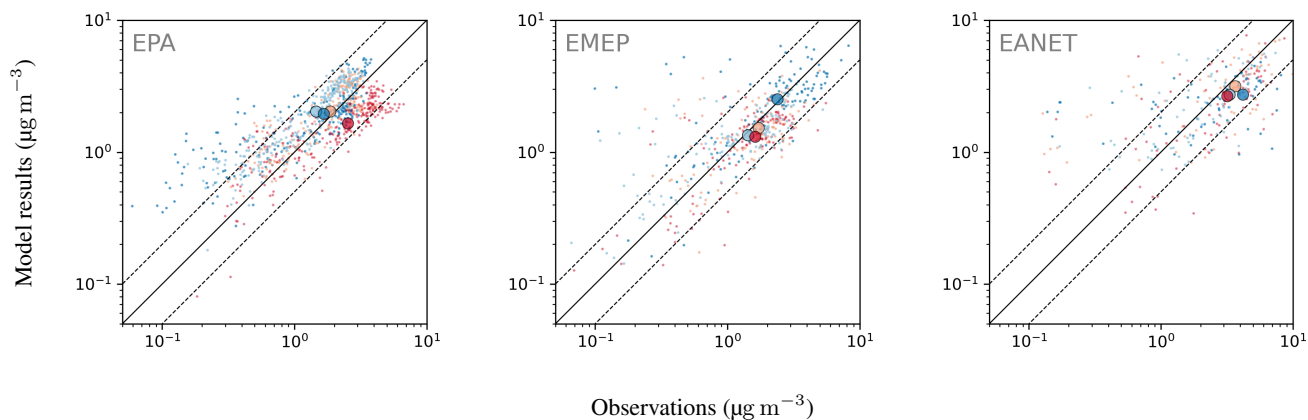
Figure 20. Scatter plots of observed and simulated monthly average SO_4^{2-} concentrations for the year 2010 and three observational networks: EPA, EMEP, and EANET (left to right). The coloring of the points represents a categorization into seasons (dark blue: DJF, orange: MAM, red: JJA, light blue: SON), the respective seasonal averages of monthly concentrations are depicted as large circles. Dashed lines denote the interval of a factor of 2 of the observations. The simulated concentrations were obtained by sampling the modeled data at the respective station locations using bilinear interpolation over neighbouring grid points.
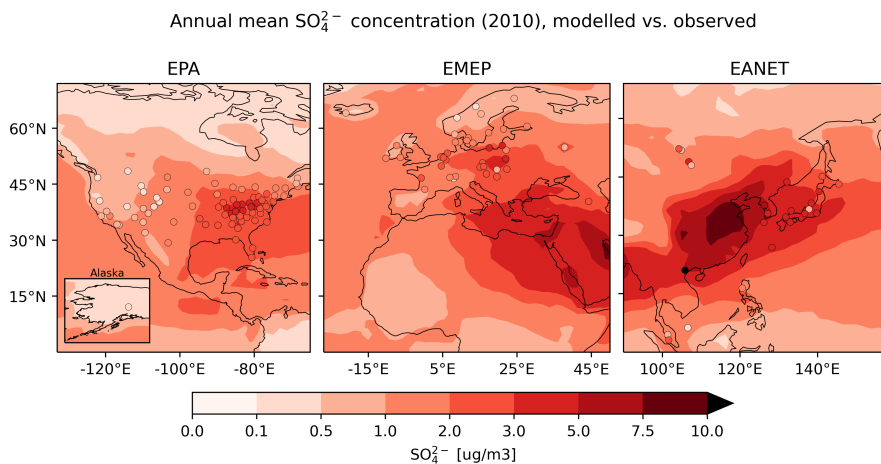
Figure 21. Annual mean SO_4^{2-} concentrations for the year 2010 for the model and three observational networks: EPA, EMEP, and EANET (left to right). Simulated data are shown as shaded contours, while the observational data are depicted as circles.
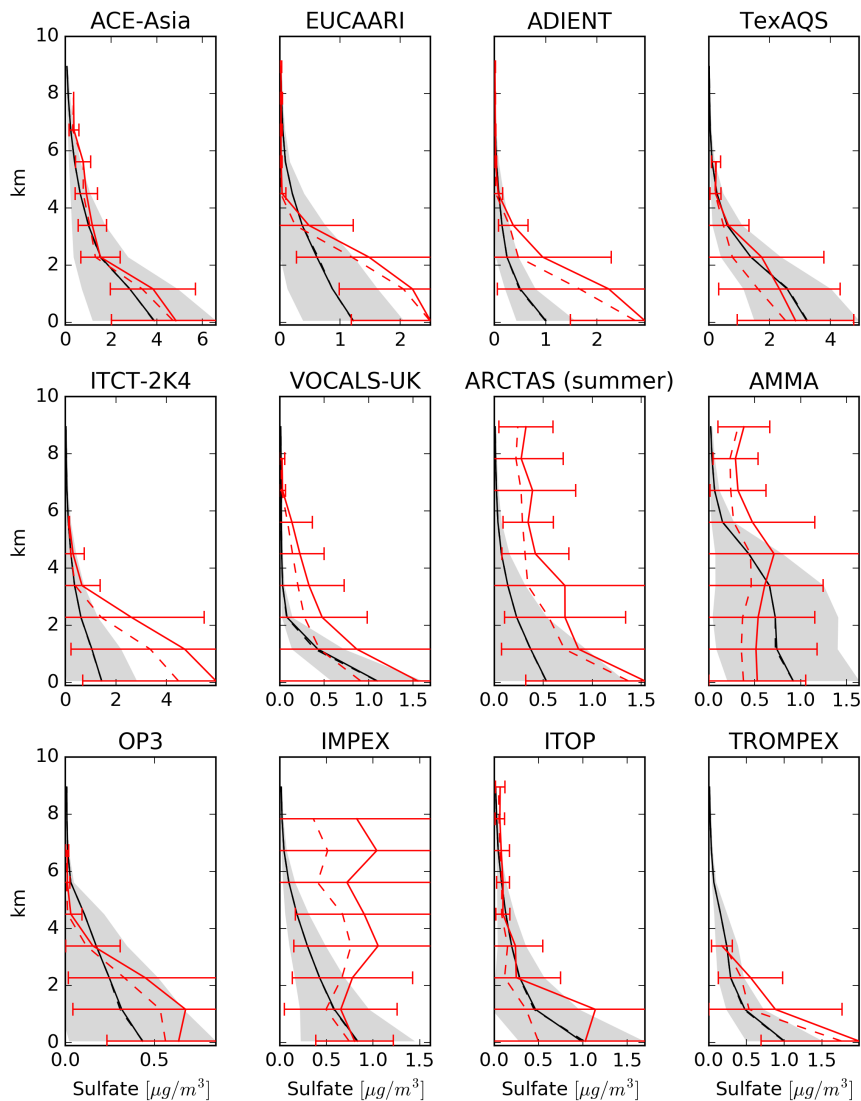
Figure 22. Model results of mean vertical profile of sulfate aerosol for selected field campaigns in black, and spatio-temporal standard deviation as grey area. The observed mean values are depicted in solid red, with the bars representing the standard deviation of the observations. The observed median is presented as red dashed line.

4.6.2 Nitrate (NO_3^-)

Nitrate is less well represented than sulfate, showing a general overestimation of observed concentrations with an average ratio of simulated to observed concentrations by at least 3.75. This comparably large ratio is dominated by a few stations with small concentrations, where the median ratios lie between 1.70 and 2.84. About half (EMEP) to two thirds (EPA, EANET)

of the simulated monthly mean concentrations exceed a factor of 2 with respect to the observations. For EANET and EMEP, the number of monitoring stations is substantially lower than for EPA, which may partly explain the larger spread in both, the model results and observations (OSTD, MSTD). The RMSE is larger than the observed standard deviations for all considered networks, suggesting a less faithful representation of this species. This overestimation may be attributed to the usage of Teflon filters, as nitrate can evaporate from the filters under warm and dry conditions (Ames and Malm, 2001). Schaap (2003), Schaap et al. (2004) and de Meij et al. (2006) showed that particulate ammonium and nitrate partially evaporate from the filters at temperatures between 15 to 20°C and can evaporate completely at temperatures above 20°C. Therefore, this effect predominantly affects measurements during the warmer seasons, when nitrate concentrations are close to the annual minimum. An indication for overestimation due to evaporation would then be a closer agreement between model and observation in the colder winter months. However, both in relative and absolute terms, the overestimation of monthly mean nitrate concentrations is more pronounced in winter than in summer for the three considered networks (Figure 23). All regions show the same seasonal cycle with respect to averaged monthly mean concentrations; a maximum in winter and a minimum in summer, both for model results and observations. The spatial gradient of annual mean concentrations is captured well for North America (EPA), although the concentrations towards the East coast are generally overestimated. The low number of monitoring stations for EANET and EMEP does not allow us to draw solid conclusions; yet we can report that the North-South gradient of nitrate over Europe is reproduced by the model, except for an outlier at high altitude in Central Europe (Figure 24). The region with highest simulated annual mean concentrations and strong spatial gradients is East Asia, however it is scarcely covered by monitoring stations reporting full coverage for the considered year 2010.
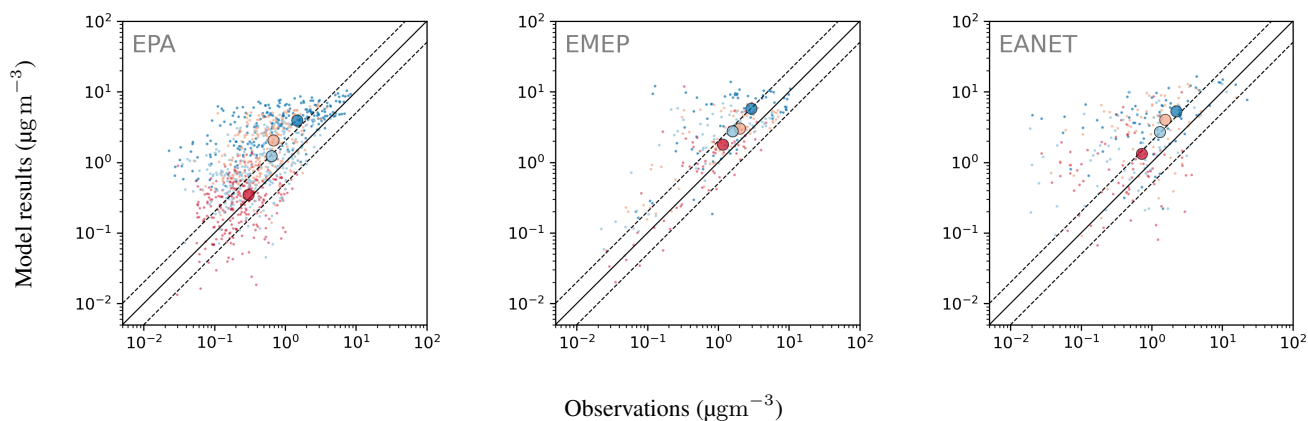
Figure 23. As in Figure 20, but for NO_3^-.

4.6.3 Ammonium (NH_4^+)

Considering the ratio of averaged monthly mean ammonium concentrations, the model overestimates the observed concentrations, yet to a lower degree than for nitrate (Table 6). This feature is also apparent in the fraction of simulated monthly

Annual mean NO_3^- concentration (2010), modelled vs. observed
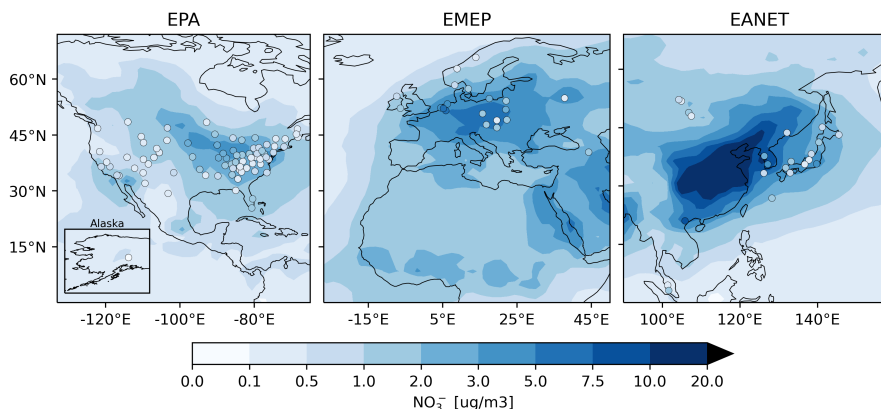
Figure 24. As in Figure 21, but for NO_3^-.

mean values within a factor of two of the observations: 54.7% for the network in East Asia and more than 60% for Europe
590   and North America. The magnitude of overestimation is similar for the three networks, ranging from 40% to 50%. RMSE
values are close to the standard deviation of observations in all networks, again indicating a good representation by the model.
The largest concentrations occur during the winter months (Figure 25). While the degree of overestimation is similar for the
different seasons in EMEP and EANET, this does not hold for EPA: summer concentrations are systematically underestimated,
whereas autumn to spring concentrations are generally overestimated. The monthly mean concentrations for winter and spring
595   constitute most of the values outside the factor of 2 regarding the observations for all considered regions. Both the observed
North-South and East-West gradients of annual mean concentrations are represented well for the EPA network ((Figure 26),
though the simulated gradient is less pronounced.

The North-South gradient of observations over Europe is also captured by the model, although the number of stations is
again comparably low. The simulated spatial patterns in East Asia also match the observations arguably well.

600   ### 4.6.4   Dust and sea spray

This section provides an overview for species frequently found in dust and sea spray aerosol: sodium, calcium, magnesium,
potassium and chloride. As the ocean is a large source of these water-soluble species, concentrations over the sea and coastal
areas are large, as opposed to lower concentrations over the continents. Sodium, potassium, magnesium and calcium can also
be found in desert dust, for instance in the Sahara, as reported by Reid et al. (2003) and Moreno et al. (2006). However, most
605   of the monitoring locations except for those in coastal areas are sampling quite remote sites far from the source regions, and
thus can not be expected to display the full range of concentrations. In the following, we present the results for sodium in more
detail, followed by a brief overview of the remaining species.
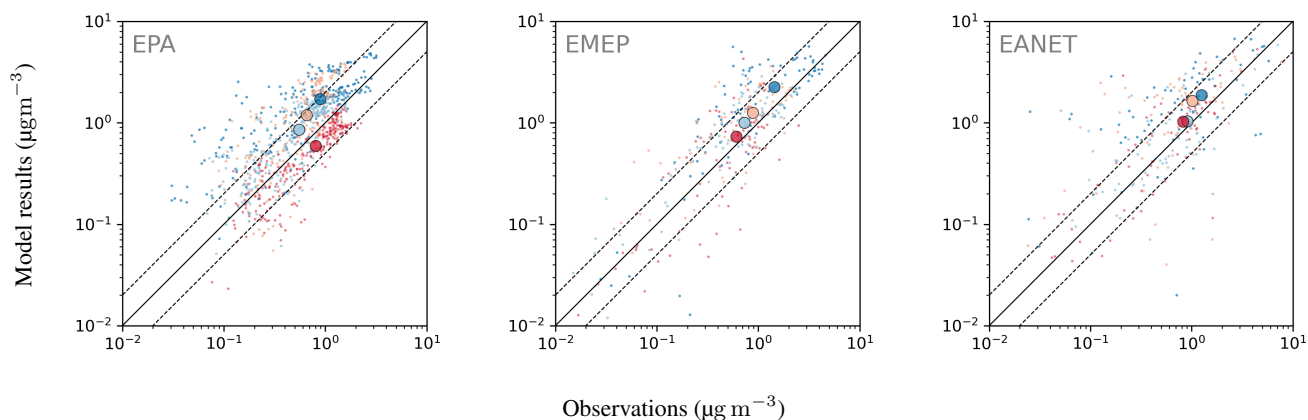
Figure 25. As in Figure 20, but for NH_4^+.
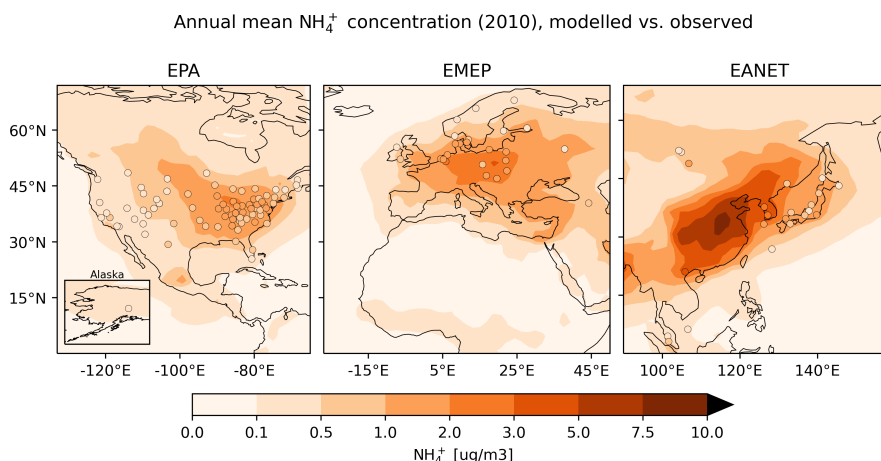
Figure 26. As in Figure 21, but for NH_4^+.

Sodium is represented well by the model, as averaged monthly mean concentrations from model and observations agree in general, particularly for EPA (Table 6). The mean ratio MM/OM, however, shows an average overestimation by a factor of at least 2. The observational standard deviation OSTD for all regions is smaller than the RMSE, the latter being reduced compared to the results from a previous study by Pozzer et al. (2012a). For EMEP, more than 3 out of 5 simulated monthly mean values lie within a factor of 2 of the observations and more than 53% and 46% for EMEP and EANET, respectively, which is a substantial improvement compared to Pozzer et al. (2012a). The latter two networks offer again only a small number of stations. Considering the average of monthly mean concentrations separated by season, one can observe an underestimation of summer concentrations for all networks (Figure 27).

As mentioned before, the regional distribution of stations does not cover those regions with high concentrations. However, including the information of all networks at once, one can observe that continental stations exhibit low annual mean concentrations, while high concentrations can be observed for instance at stations close to the coast (i.e. Japan, Florida, Denmark, Sweden), indicating that spatial features of the global sodium distribution are qualitatively captured (Figure 28).

620 Potassium, magnesium and calcium ions share spatial features with sodium in the model, exhibiting elevated values over the ocean, as well as over the Sahara and Gobi desert, and reduced concentrations over other continental areas.

The number of stations in EANET is quite low for all sea spray species which, on the one hand, allows for a few outliers to dominate mean values and errors. On the other hand, EPA offers a large number of stations, yet the correspondence of model and observations is also quite low for sea spray and dust species. Average monthly mean concentrations for magnesium are 625 represented well in the model, which is caused by a large overestimation of concentrations in winter months balancing an underestimation of summer concentrations (not shown).

Chloride concentrations are widely overestimated with respect to all three networks. The exceptionally high ratio $\overline{MM/OM}$ for EMEP is caused by two outliers with MM/OM > 1000 due to very low observed concentrations. Without these, $\overline{MM/OM}$ is better, with a value of 13.08.
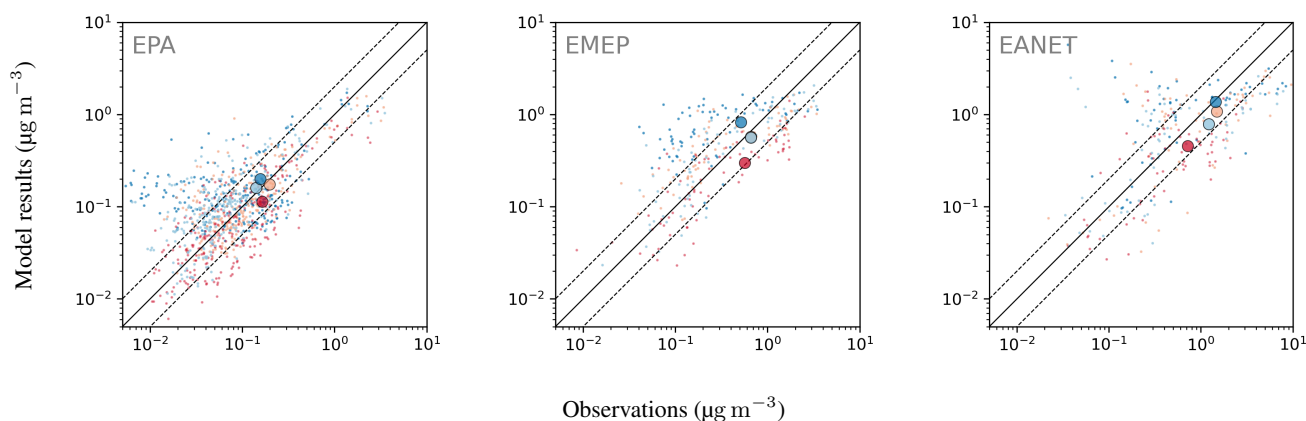
Figure 27. As in Figure 20, but for Na^+.

630 ### 4.6.5 Organic Aerosols (OA)

Figure 30 shows the comparison of model calculated OA concentrations with measurements from the EMEP observational network over Europe, the IMPROVE network over rural North American locations, as well as short-term measurement data collected over East Asia as summarized by Jo et al. (2013). As we used only measurements taken in the year 2010, a low number of observations are present for East Asia, and the comparison must be taken cautiously for this region. The comparison 635 statistic is presented in Tab. 6. The model captures relatively well the monthly average concentrations of OA over these highly populated regions of the Northern Hemisphere. This is rather encouraging, given the expected uncertainties of the emission

Annual mean Na⁺ concentration (2010), modelled vs. observed
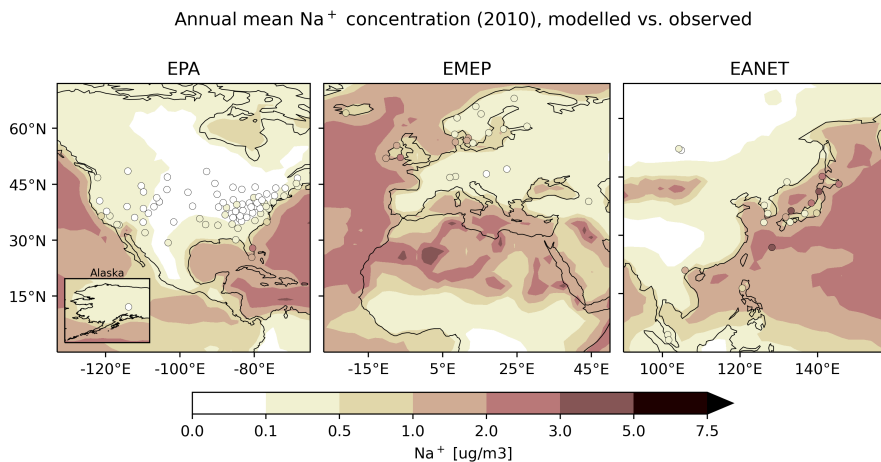
Figure 28. As in Figure 21, but for Na^+.
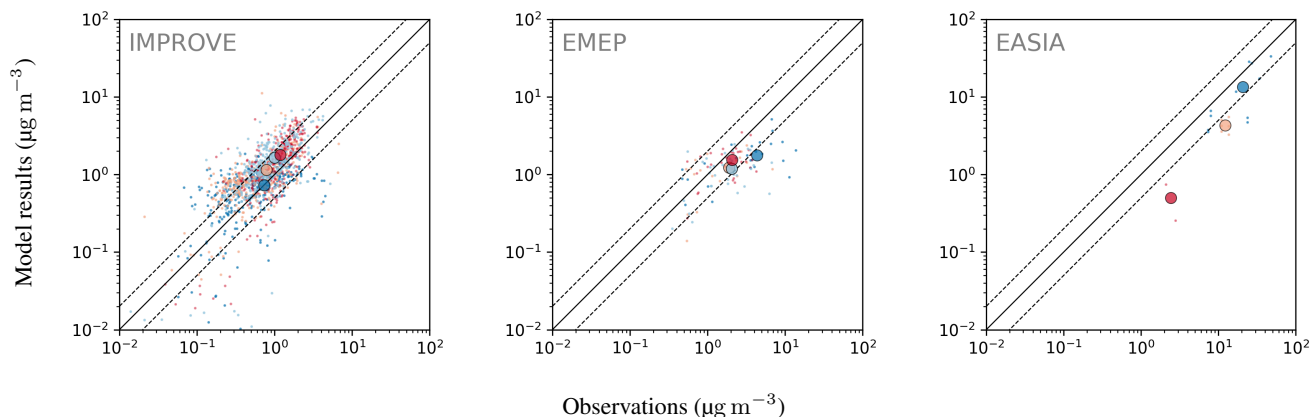
Figure 29. As in Figure 20, but for OA.

inventory and the complex chemistry involved to simulate the secondary organic aerosol formation. It is worth emphasizing that the model considers the formation of SOA solely from the homogeneous gas-phase photochemical oxidation of its precursors. Therefore, the omission of other SOA formation pathways (e.g., from aqueous-phase and heterogeneous reactions) can add to the model bias. This is mostly evident during winter (e.g., over Europe), when the relative importance of these processes on SOA formation is increasing due to the lower photochemical activity and the limited conversion of gas phase organic precursors to SOA. In addition, recent studies have provided strong evidence that the uptake of water-soluble gas-phase oxidation products (even small carbonyls like formaldehyde and acetic acid) can be the main driver of SOA pollution during haze events over Eastern Asia (Gkatzelis et al., 2020). Given the coarse resolution of the model and its inability to simulate these SOA formation pathways, the observed total OA concentrations are expected to be systematically underestimated by the model over Eastern
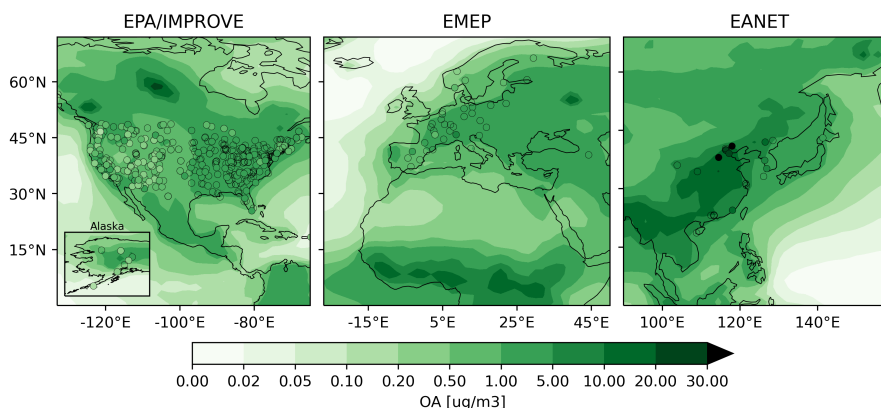
Figure 30. As in Figure 21, but for OA.

and Southern Asia. Nevertheless, model results are in general in reasonable agreement with observations with the exception of the strong underestimation over Beijing and Shijiazhuang, which brings the $\overline{MM/OM}$ to very low value (i.e. 0.51). As pointed out by Miao et al. (2021) and Zhao et al. (2016), the emission inventories for semivolatile and intermediate volatility organic compounds are insufficient and lead to the majority of the model biases in simulating OA in these regions that are influenced significantly by anthropogenic emissions.

Over Europe, the model also underestimates OA, with $\overline{MM/OM}$ of 0.83 (see Tab. 6). The model performs worst during winter. Tsimpidi et al. (2016) has identified the lack of biomass burning emissions as the main source of this discrepancy over Europe. Later, Kodros et al. (2020) and Paglione et al. (2020) have shown evidence that biomass burning also contributes significantly to SOA formation during wintertime following its oxidation by the NO_3 radical in the dark. Over North America, the model overestimates OA over rural areas with a $\overline{MM/OM}$ equal to 1.73. However, as shown in Fig. 29, part of this discrepancy is explained by the low values of OA over the US national parks.

Despite the agreement of the surface OA concentrations between model results and observations, the OA are strongly underestimated in the free troposphere. In Fig. 31, the model is compared with 12 field campaign measurements (Heald et al., 2011). Our results show similar agreement to the one obtained by Heald et al. (2011), with the simulated values below the observed one.

5   Conclusions

We have presented an evaluation of EMAC with a comprehensive degradation scheme for organics (MOM) in the MECCA chemistry submodel, combined with an explicit estimation of the organic tracers' condensation on aerosols with a VBS approach (ORACLE submodel). We have compared the model results with a large number of in-situ and satellite based remote sensing observations. The evaluation focuses on carbon monoxide (CO), simple organics and aerosols, which are most in-
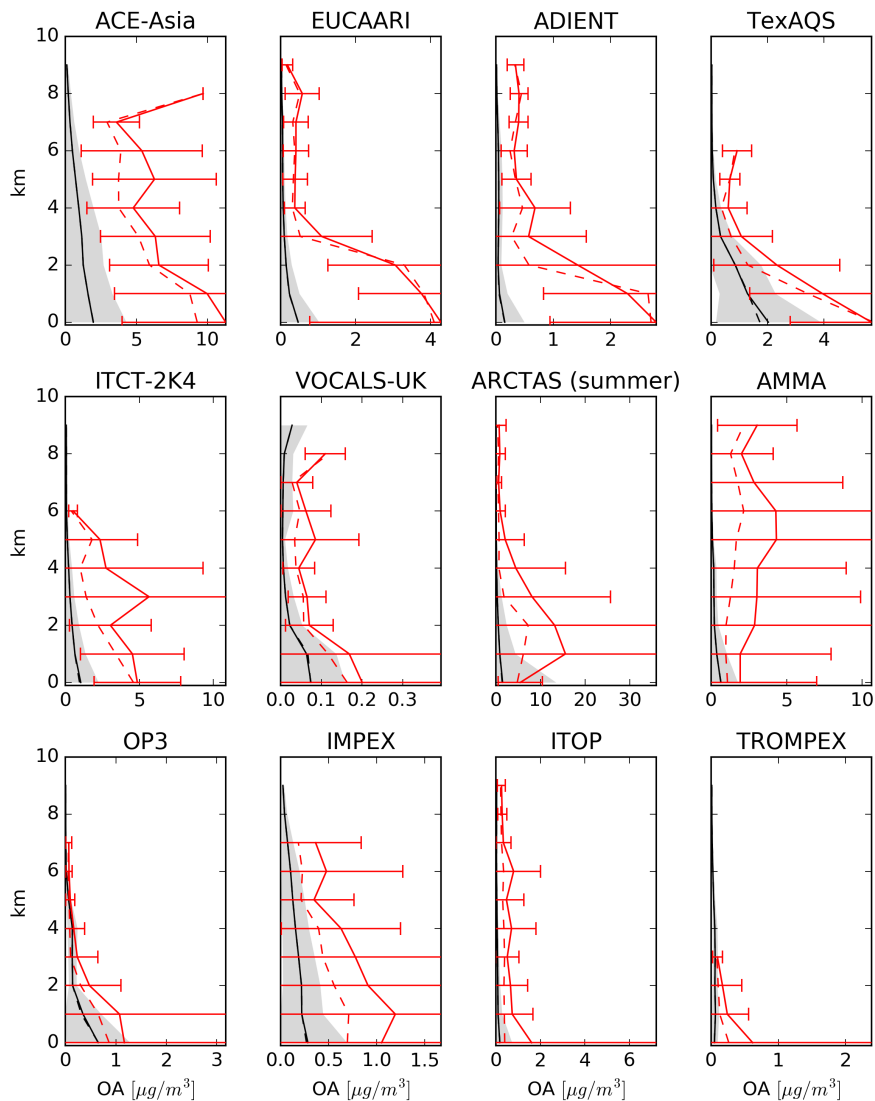
Figure 31. As Fig.22, but for organic aerosol.

fluenced by the new scheme. CO is correctly reproduced compared with station measurements, with the correct north-south gradient. Nevertheless, once the model results are compared with the satellite observations from MOPITT, an overestimation of CO over the Amazon basin is apparent, especially in autumn, possibly due to an overestimation of the biomass burning emissions simulated by the model. For alkanes the comparison shows a good agreement, although an oceanic source for the butanes is missing. In contrast, the model underestimates alkenes, and especially C_3H_6, which shows large differences compared to the observations. Model results of oxygenated species show an indifferent picture when compared to observations,

depending on the tracer: while methanol is well reproduced, simulated acetone shows large spatial discrepancies compared to the remotely sensed observations. In fact, for the latter, the model misses strong emissions over the boreal forests, while it predicts instead too high total columns over tropical forests (i.e., Amazonia and Central Africa). Formic and acetic acid show similar agreements to the observations, with the main tropical sources well reproduced, but with a strong underestimation elsewhere.

The aerosols at the surface are well reproduced by the model, both with respect to composition and total amount. The annually averaged simulated AODs show a very good agreement with the AERONET station observations, but with some deficiencies in the representation of the short term variability. The agreement of the fine particulate mass ($PM_{2.5}$) near the surface is also quite good, with most of the simulated values within a factor of 2 to the observations. The evaluation of the aerosol chemical composition shows a high level of agreement for near-surface sulphate and some more deviations for NH_4^+ and nitrate, which are both overestimated by the model, especially the latter (even though the observations are characterized with a high level of uncertainty). The mechanically produced primary aerosol species (dust and seasalt) show a reasonable agreement with the observations with some substantial overestimation of the simulated chloride concentrations indicating a too weak acid displacement process over the continents.

Finally, the comparison of OA shows a good agreement with station observations, while the vertical distribution of the simulated values are largely underestimated, when compared with aircraft measurements, analogously to other global atmospheric chemistry models of similar complexity, although significant improvement in this direction has been recently published (Pai et al., 2020).

6 Outlook

The presented model evaluation is useful for identifying areas for further model improvements. A few possible directions are discussed next.

Emissions have always been a critical point for simulating tropospheric chemistry. It has already been shown in many studies that even anthropogenic emissions of alkanes need to be improved as severely underestimated in many inventories (e.g. Emmons et al., 2015; Tilmes et al., 2016), mostly coming from erroneous speciation of the total VOC emissions (Dalsøren et al., 2018)

Residential wood burning and/or biofuel use (e.g., for heating) that often contribute significantly to both POA and SOA formation over urban areas are strongly underestimated in the emission inventories (Tsimpidi et al., 2016; Denier Van Der Gon et al., 2015). In addition, global models lack OA emissions from residential and commercial cooking activities that can be an important source of OA (Mohr et al., 2012; Sun et al., 2011; Ge et al., 2012; Hayes et al., 2013). Underestimation of cold-start vehicle emissions (Weilenmann et al., 2009) can also lead to significant underestimation of OA formation from the transport sector (e.g., during wintertime).

As seen in this study, the model results underestimate selected VOCs in boreal regions. The thawing of permafrost is potentially an additional emission source of organic compounds at high latitudes in the northern hemisphere (Li et al., 2020), which

has not been considered yet. However, an estimate with global data sets is still missing. Furthermore, the emission of VOCs from biomass burning is likely strongly underestimated. In fact, overwintering fires in boreal forest (Scholten et al., 2021), which smoulder through the non-fire season, are normally not detected by satellite observations and therefore are missing in our used emissions dataset. Moreover, peat fires are not easily detected from space, but are characterized by larger emission factors for many VOCs. They are important for simulating air composition during peat fires in Indonesia (Rosanka et al., 2021a) and likely critical for resolving the model biases at high latitudes, where most of peatland is located and could be further released by permafrost thawing. Ramo et al. (2021) also found that small undetected fires enhance the estimated amount of emitted carbon from biomass burning in sub-Saharan Africa by 31-101% . Finally, soil temperature and soil wetness play an important role in the estimation of the online emissions of biogenic VOCs, and it is therefore important to have a correct simulation of the surface properties by the underlying climate model.

Furthermore, dry deposition is a relevant process also affecting VOCs in the lower troposphere (Khan et al., 2015). The inclusion of the additional uptake at the plant cuticle leads to a better representation (Karl et al., 2004; Müller et al., 2018; Emmerichs et al., 2021) and would likely reduce the overestimation of species like acetaldehyde in the Tropics, as shown here. In the Amazon forest, the missing storage capacity of soil water leading to too high temperatures (Hagemann and Stacke, 2015) additionally causes an underestimation of dry deposition (Emmerichs et al., 2021), while temperature-dependent processes like VOC emissions are overestimated.

Another source of uncertainty is related to the scavenging efficiency of gas-phase OA precursors. The water solubility of these oxidized organic vapors is largely unknown and is typically considered uniform for all organic compounds in modeling studies even though they become increasingly more hydrophilic during their atmospheric lifetime (Hodzic et al., 2014; Tsimpidi et al., 2017).

The extension of MOM for the oxidation of additional VOCs has the potential to reduce the negative model biases for some oxygenated volatile organic compounds (OVOCs) and enhance the predicted OA levels. For instance, with an emission strength of more than $40 \, \mathrm{Tg \, yr^{-1}}$, anthropogenic C_5- and higher hydrocarbons can be a significant source of OVOCs like acetaldehyde and acetone (Pozzer et al., 2010). Further improvements are expected from an extended representation of the emission and oxidation of known biogenic VOCs with more than 5 carbon atoms. Moreover, the emissions of aromatic compounds from biogenic sources could be as large as $40 \, \mathrm{Tg \, yr^{-1}}$ (Misztal et al., 2015). So far only a small emission of toluene is considered and a more comprehensive representation of biogenic aromatics would likely lead to further improvements.

The formation of SOA in most models relies on the reaction of its gas-phase precursors with reactive atmospheric radicals (e.g., OH, O_3, NO_3) and their chemical aging is usually considered by the further photo-oxidation of the semivolatile products solely in the gas phase. However, SOA is also subject to oxidation in the aqueous phase through superficial and bulk interactions with gas-phase oxidants (George and Abbatt, 2010). Therefore, fundamental processes of SOA formation in the aqueous phase (e.g., from isoprene epoxydiols (Nguyen et al., 2009) and glyoxal (Fu et al., 2008)) are typically missing from the conventionally used parameterizations. In addition, the uptake of small carbonyls (e.g., aldehydes and acids) to the aqueous phase and their subsequent oxidation and oligomerization has been recently linked to significant increases of SOA mass during pollution events (Gkatzelis et al., 2021).

Recently, MOM has been coupled to the detailed Jülich Aqueous-phase Mechanism of Organic Chemistry (JAMOC, Rosanka et al., 2021c) for cloud droplets. An explicit treatment of multiphase chemistry of OVOC has already been used for assessing the global role of clouds as a sink of ozone (Rosanka et al., 2021b). By comparing EMAC's prediction of total methanol columns to IASI satellite retrievals (comparable to Sect. 4.2.3 and Fig. 8), they find that EMAC's tendency to overestimate methanol is partially reduced by the additional cloud sink. This suggests that the missing representation of in-cloud OVOC chemistry introduces a significant bias in the present study, and therefore a more detailed multi-phase chemistry should be included for future studies. Furthermore, JAMOC is limited to the oxidation of OVOCs containing up to four carbon atoms (Rosanka et al., 2021c), and an expansion to larger species (i.e. containing more than four carbon atoms) is thus desirable, in order to improve the representation of these OVOCs in EMAC when using MOM. Based on the results of Franco et al. (2021), more detailed in-cloud chemistry could improve the representation of acids (such as acetic and formic acid), which is clearly underestimated here where cloud chemistry is important.

Finally, the MOM+ORACLE framework calculates the phase partitioning of organic compounds by assuming a bulk equilibrium, without any kinetic limitation. However, the phase state of the organic aerosol can affect the mixing time of the condensed organic compounds within the aerosol. In general, equilibrium partitioning to the particle phase is a reasonable assumption if the aerosol is liquid, however, if the phase state is solid, non-equilibrium partitioning should be considered. Shiraiwa et al. (2017) suggests that kinetic limitations in the bulk may not significantly affect SOA partitioning in the boundary layer, justifying the use of equilibrium partitioning in this part of the atmosphere, but kinetic limitations should be implemented and investigated for the free and upper troposphere.

Code and data availability. The Modular Earth Submodel System (MESSy) is continuously further developed and applied by a consortium of institutions. The usage of MESSy and access to the source code is licensed to all affiliates of institutions which are members of the MESSy Consortium. Institutions can become a member of the MESSy Consortium by signing the MESSy Memorandum of Understanding. More information can be found on the MESSy Consortium Website (http://www.messy-interface.org). The code presented here has been based on MESSy version 2.54 and is available in the official release of version 2.55.

Author contributions. A.P., A.P.T. and V.A.K. planned the research. A.P. designed, coded, prepared the input files and performed the model simulation. A.P., V.K., S.G., S.F.R., B.F. S.R., T.E., D.T., H.T., V.F., A.P.T. and M.K. wrote the manuscript. D.T. developed MOM and integrated it into MECCA. S.G. implemented extended budgeting of species turnover. A.P.T and V.A.K. modified ORACLE to accommodate the organic tracers from the MOM chemical mechanism. A.P.T. compared model results to surface OA observations. M.C., D.G. and J.K. provided the emissions for the simulations. A.P., S.F.R, V.K, D.A. and M.K have contributed to the evaluation. C.H. provided observational data for the comparison. P.J. and H.T. contributed to model development of the here applied system. B.F., L.C. and P-F.C. developed the IASI VOC products and performed the comparisons with EMAC.

770 *Competing interests.* No competing interests are present.

Acknowledgements. IASI is a joint mission of Eumetsat and the Centre National d'Etudes Spatiales (CNES, France). The IASI Level–1C data are distributed in near real-time by Eumetsat through the EumetCast distribution system. The authors acknowledge the AERIS data infrastructure (https://www.aeris-data.fr/, last access on September 21, 2021) for providing access to the IASI Level–1C data and Level–2 temperature data. IASI activities have been supported by the Belgian State Federal Office for Scientific, Technical and Cultural Affairs

775 (Prodex arrangement IASI.FLOW). L. Clarisse is a research associate supported by the F.R.S.–FNRS. H.T. acknowledges funding from the Carl-Zeiss foundation. We are grateful to Colette Heald for providing the aircraft data and for her support and suggestions to improve the manuscript.

References

Akagi, S., Yokelson, R. J., Wiedinmyer, C., Alvarado, M., Reid, J., Karl, T., Crounse, J., and Wennberg, P.: Emission factors for open and domestic biomass burning for use in atmospheric models, Atmospheric Chemistry and Physics, 11, 4039–4072, 2011.

Allen, H., Crounse, J., Kim, M., Teng, A., and Wennberg, P.: ATom: L2 In Situ Data from Caltech Chemical Ionization Mass Spectrometer (CIT-CIMS), https://doi.org/10.3334/ORNLDAAC/1713, https://daac.ornl.gov/cgi-bin/dsviewer.pl?ds_id=1713, 2019.

Ames, R. B. and Malm, W. C.: Comparison of sulfate and nitrate particle mass concentrations measured by IMPROVE and the CDN, Atmospheric Environment, 35, 905 – 916, https://doi.org/https://doi.org/10.1016/S1352-2310(00)00369-1, http://www.sciencedirect.com/science/article/pii/S1352231000003691, 2001.

Andreae, M. O.: Emission of trace gases and aerosols from biomass burning–an updated assessment, Atmospheric Chemistry and Physics, 19, 8523–8546, 2019.

Apel, E., Asher, E., Hills, A., and Hornbrook, R.: ATom: Volatile Organic Compounds (VOCs) from the TOGA instrument, Version 2, https://doi.org/10.3334/ORNLDAAC/1936, https://daac.ornl.gov/cgi-bin/dsviewer.pl?ds_id=1936, 2021.

Astitha, M., Lelieveld, J., Abdel Kader, M., Pozzer, A., and de Meij, A.: Parameterization of dust emissions in the global atmospheric chemistry-climate model EMAC: impact of nudging and soil properties, Atmospheric Chemistry and Physics, 12, 11 057–11 083, https://doi.org/10.5194/acp-12-11057-2012, https://acp.copernicus.org/articles/12/11057/2012/, 2012.

Barletta, B., Biggs, B., Blake, D., Blake, N., Hoffman, A., Hughes, S., Meinardi, S., Vieznor, N., and Woods, C.: ATom: L2 Halocarbons and Hydrocarbons from the UC-Irvine Whole Air Sampler (WAS), https://doi.org/10.3334/ORNLDAAC/1751, https://daac.ornl.gov/cgi-bin/dsviewer.pl?ds_id=1751, 2019.

Barna, M. and Lamb, B.: Improving ozone modeling in regions of complex terrain using observational nudging in a prognostic meteorological model, Atmospheric Environment, 34, 4889 – 4906, https://doi.org/https://doi.org/10.1016/S1352-2310(00)00231-4, http://www.sciencedirect.com/science/article/pii/S1352231000002314, 2000.

Bates, K. H., Jacob, D. J., Wang, S., Hornbrook, R. S., Apel, E. C., Kim, M. J., Millet, D. B., Wells, K. C., Chen, X., Brewer, J. F., Ray, E. A., Commane, R., Diskin, G. S., and Wofsy, S. C.: The Global Budget of Atmospheric Methanol: New Constraints on Secondary, Oceanic, and Terrestrial Sources, Journal of Geophysical Research: Atmospheres, 126, https://doi.org/10.1029/2020jd033439, 2021.

Berrisford, P., Dee, D., Poli, P., Brugge, R., Fielding, M., Fuentes, M., Kållberg, P., Kobayashi, S., Uppala, S., and Simmons, A.: The ERA-Interim archive Version 2.0, p. 23, https://www.ecmwf.int/node/8174, 2011.

Bloss, C., Wagner, V., Jenkin, M. E., Volkamer, R., Bloss, W. J., Lee, J. D., Heard, D. E., Wirtz, K., Martin-Reviejo, M., Rea, G., Wenger, J. C., and Pilling, M. J.: Development of a detailed chemical mechanism (MCMv3.1) for the atmospheric oxidation of aromatic hydrocarbons, Atmospheric Chemistry and Physics, 5, 641–664, https://doi.org/10.5194/acp-5-641-2005, https://acp.copernicus.org/articles/5/641/2005/, 2005.

Cabrera-Perez, D., Taraborrelli, D., Sander, R., and Pozzer, A.: Global atmospheric budget of simple monocyclic aromatic compounds., Atmospheric Chemistry & Physics, 16, 2016.

Capouet, M., Müller, J.-F., Ceulemans, K., Compernolle, S., Vereecken, L., and Peeters, J.: Modeling aerosol formation in alpha-pinene photo-oxidation experiments, Journal of Geophysical Research: Atmospheres, 113, https://doi.org/https://doi.org/10.1029/2007JD008995, 2008.

Carter, T. S., Heald, C. L., Jimenez, J. L., Campuzano-Jost, P., Kondo, Y., Moteki, N., Schwarz, J. P., Wiedinmyer, C., Darmenov, A. S., Silva, A. M. d., et al.: How emissions uncertainty influences the distribution and radiative impacts of smoke from fires in North America, Atmospheric Chemistry and Physics, 20, 2073–2097, 2020.

Clerbaux, C., Boynard, A., Clarisse, L., George, M., Hadji-Lazaro, J., Herbin, H., Hurtmans, D., Pommier, M., Razavi, A., Turquety, S., Wespes, C., and Coheur, P.-F.: Monitoring of atmospheric composition using the thermal infrared IASI/MetOp sounder, Atmospheric Chemistry and Physics, 9, 6041–6054, https://doi.org/10.5194/acp-9-6041-2009, 2009.

Crippa, M., Guizzardi, D., Muntean, M., Schaaf, E., Dentener, F., van Aardenne, J. A., Monni, S., Doering, U., Olivier, J. G. J., Pagliari, V., and Janssens-Maenhout, G.: Gridded emissions of air pollutants for the period 1970–2012 within EDGAR v4.3.2, Earth Syst. Sci. Data, 10, 1987–2013, https://doi.org/10.5194/essd-10-1987-2018, https://www.earth-syst-sci-data.net/10/1987/2018/, 2018.

Crutzen, P. J. and Lawrence, M. G.: The impact of precipitation scavenging on the transport of trace gases: A 3-dimensional model sensitivity study, Journal of Atmospheric Chemistry, 37, 81–112, 2000.

Dalsøren, S. B., Myhre, G., Hodnebrog, Ø., Myhre, C. L., Stohl, A., Pisso, I., Schwietzke, S., Höglund-Isaksson, L., Helmig, D., Reimann, S., et al.: Discrepancy between simulated and observed ethane and propane levels explained by underestimated fossil emissions, Nature Geoscience, 11, 178–184, 2018.

de Meij, A., Krol, M., Dentener, F., Vignati, E., Cuvelier, C., and Thunis, P.: The sensitivity of aerosol in Europe to two different emission inventories and temporal distribution of emissions, Atmospheric Chemistry and Physics, 6, 4287–4309, https://doi.org/10.5194/acp-6-4287-2006, https://acp.copernicus.org/articles/6/4287/2006/, 2006.

Deeter, M. N., Edwards, D. P., Francis, G. L., Gille, J. C., Mao, D., Martínez-Alonso, S., Worden, H. M., Ziskin, D., and Andreae, M. O.: Radiance-based retrieval bias mitigation for the MOPITT instrument: the version 8 product, Atmospheric Measurement Techniques, 12, 4561–4580, https://doi.org/10.5194/amt-12-4561-2019, https://amt.copernicus.org/articles/12/4561/2019/, 2019.

Denier Van Der Gon, H., Bergström, R., Fountoukis, C., Johansson, C., Pandis, S., Simpson, D., and Visschedijk, A. J.: Particulate emissions from residential wood combustion in Europe–revised estimates and an evaluation, Atmospheric Chemistry and Physics, 15, 6503–6519, 2015.

Dietmüller, S., Jöckel, P., Tost, H., Kunze, M., Gellhorn, C., Brinkop, S., Frömming, C., Ponater, M., Steil, B., Lauer, A., and Hendricks, J.: A new radiation infrastructure for the Modular Earth Submodel System (MESSy, based on version 2.51), Geoscientific Model Development, 9, 2209–2222, https://doi.org/10.5194/gmd-9-2209-2016, https://gmd.copernicus.org/articles/9/2209/2016/, 2016.

Donahue, N. M., Epstein, S., Pandis, S. N., and Robinson, A. L.: A two-dimensional volatility basis set: 1. organic-aerosol mixing thermodynamics, Atmospheric Chemistry and Physics, 11, 3303–3318, 2011.

Dubovik, O., Smirnov, A., Holben, B., King, M., Kaufman, Y., Eck, T., and Slutsker, I.: Accuracy assessments of aerosol optical properties retrieved from Aerosol Robotic Network (AERONET) Sun and sky radiance measurements, J. Geophys. Res, 105, 9791–9806, 2000.

Dufour, G., Szopa, S., Harrison, J. J., Boone, C. D., and Bernath, P. F.: Seasonal variations of acetone in the upper troposphere–lower stratosphere of the northern midlatitudes as observed by ACE-FTS, Journal of Molecular Spectroscopy, 323, 67–77, https://doi.org/10.1016/j.jms.2016.02.006, 2016.

E. Jenkin, M., Shallcross, D. E., and Harvey, J. N.: Development and application of a possible mechanism for the generation of cis-pinic acid from the ozonolysis of α and β - pinene, Atmospheric Environment, 34, 2837 – 2850, http://www.sciencedirect.com/science/article/pii/S135223100000087X, 2000.

Emmerichs, T., Kerkweg, A., Ouwersloot, H., Fares, S., Mammarella, I., and Taraborrelli, D.: A revised dry deposition scheme for land–atmosphere exchange of trace gases in ECHAM/MESSy v2.54, Geoscientific Model Development, 14, 495–519, https://doi.org/10.5194/gmd-14-495-2021, https://gmd.copernicus.org/articles/14/495/2021/, 2021.

Emmons, L., Arnold, S., Monks, S., Huijnen, V., Tilmes, S., Law, K. S., Thomas, J. L., Raut, J.-C., Bouarar, I., Turquety, S., et al.: The POLARCAT Model Intercomparison Project (POLMIP): overview and evaluation with observations, Atmospheric Chemistry and Physics, 15, 6721–6744, 2015.

Emmons, L. K., Hauglustaine, D. A., Müller, J.-F., Carroll, M. A., Brasseur, G. P., Brunner, D., Staehelin, J., Thouret, V., and Marenco, A.: Data composites of airborne observations of tropospheric ozone and its precursors, Journal of Geophysical Research: Atmospheres, 105, 20 497–20 538, 2000.

Epstein, S. A., Riipinen, I., and Donahue, N. M.: A semiempirical correlation between enthalpy of vaporization and saturation concentration for organic aerosol, Environmental science & technology, 44, 743–748, 2010.

Farina, S. C., Adams, P. J., and Pandis, S. N.: Modeling global secondary organic aerosol formation and processing with the volatility basis set: Implications for anthropogenic secondary organic aerosol, Journal of Geophysical Research: Atmospheres, 115, https://doi.org/https://doi.org/10.1029/2009JD013046, https://agupubs.onlinelibrary.wiley.com/doi/abs/10.1029/2009JD013046, 2010.

Fischer, E., Jacob, D. J., Millet, D. B., Yantosca, R. M., and Mao, J.: The role of the ocean in the global atmospheric budget of acetone, Geophysical Research Letters, 39, 2012.

Fischer, E. V., Jacob, D. J., Yantosca, R. M., Sulprizio, M. P., Millet, D. B., Mao, J., Paulot, F., Singh, H. B., Roiger, A., Ries, L., Talbot, R. W., Dzepina, K., and Deolal, S. P.: Atmospheric peroxyacetyl nitrate (PAN): a global budget and source attribution, Atmospheric Chemistry and Physics, 14, 2679–2698, https://doi.org/10.5194/acp-14-2679-2014, 2014.

Franco, B., Clarisse, L., Stavrakou, T., Müller, J.-F., Van Damme, M., Whitburn, S., Hadji-Lazaro, J., Hurtmans, D., Taraborrelli, D., Clerbaux, C., and Coheur, P.-F.: A General Framework for Global Retrievals of Trace Gases From IASI: Application to Methanol, Formic Acid, and PAN, Journal of Geophysical Research: Atmospheres, 123, 13,963–13,984, https://doi.org/10.1029/2018jd029633, 2018.

Franco, B., Clarisse, L., Stavrakou, T., Müller, J.-F., Pozzer, A., Hadji-Lazaro, J., Hurtmans, D., Clerbaux, C., and Coheur, P.-F.: Acetone Atmospheric Distribution Retrieved From Space, Geophysical Research Letters, 46, 2884–2893, https://doi.org/10.1029/2019gl082052, 2019.

Franco, B., Clarisse, L., Stavrakou, T., Müller, J.-F., Taraborrelli, D., Hadji-Lazaro, J., Hannigan, J. W., Hase, F., Hurtmans, D., Jones, N., Lutsch, E., Mahieu, E., Ortega, I., Schneider, M., Strong, K., Vigouroux, C., Clerbaux, C., and Coheur, P.-F.: Spaceborne Measurements of Formic and Acetic Acids: A Global View of the Regional Sources, Geophysical Research Letters, 47, e2019GL086 239, https://doi.org/10.1029/2019gl086239, 2020.

Franco, B., Blumenstock, T., Cho, C., Clerbaux, C., Coheur, P.-F., Maziére, M., Smedt, I. D., Dorn, H.-P., T.Emmerichs, Fuchs, H., Gkatzelis, G., Grigffith, D., Gromov, S., Hannigan, J., Hase, F., Hohaus, T., Jones, N., Kerkweg, A., Kiendler-Scharr, A., Lutsch, E., Mahieu, E., Noveli, A., Ortega, I., Paton-Walsh, C., Pommier, M., Pozzer, A., Reimer, D., Rosanka, S., Sander, R., Schneider, M., Strong, K., Tillmann, R., Roozendael, M. V., Vereecken, L., Vigouroux, C., Wahner, A., and Taraborrelli, D.: Ubiquitous atmospheric production of organic acids mediated by cloud droplets, Nature, 593, 233–237, https://doi.org/10.1038/s41586-021-03462-x, 2021.

Fu, T.-M., Jacob, D. J., Wittrock, F., Burrows, J. P., Vrekoussis, M., and Henze, D. K.: Global budgets of atmospheric glyoxal and methylglyoxal, and implications for formation of secondary organic aerosols, Journal of geophysical research: atmospheres, 113, 2008.

Ge, X., Setyan, A., Sun, Y., and Zhang, Q.: Primary and secondary organic aerosols in Fresno, California during wintertime: Results from high resolution aerosol mass spectrometry, Journal of Geophysical Research: Atmospheres, 117, 2012.

George, I. and Abbatt, J.: Heterogeneous oxidation of atmospheric aerosol particles by gas-phase radicals, Nature Chemistry, 2, 713–722, 2010.

Gkatzelis, G. I., Papanastasiou, D. K., Karydis, V. A., Hohaus, T., Liu, Y., Schmitt, S. H., Schlag, P., Fuchs, H., Novelli, A., Chen, Q., et al.: Uptake of water-soluble gas-phase oxidation products drives organic particulate pollution in Beijing, Geophysical Research Letters, p. e2020GL091351, 2020.

Gkatzelis, G. I., Papanastasiou, D. K., Karydis, V. A., Hohaus, T., Liu, Y., Schmitt, S. H., Schlag, P., Fuchs, H., Novelli, A., Chen, Q., et al.: Uptake of Water-soluble Gas-phase Oxidation Products Drives Organic Particulate Pollution in Beijing, Geophysical Research Letters, 48, e2020GL091 351, 2021.

Grewe, V., Brunner, D., Dameris, M., Grenfell, J., Hein, R., Shindell, D., and Staehelin, J.: Origin and variability of upper tropospheric nitrogen oxides and ozone at northern mid-latitudes, Atmospheric Environment, 35, 3421–3433, 2001.

Guelle, W., Schulz, M., Balkanski, Y., and Dentener, F.: Influence of the source formulation on modeling the atmospheric global distribution of sea salt aerosol, Journal of Geophysical Research: Atmospheres, 106, 27 509–27 524, 2001.

Guenther, A., Karl, T., Harley, P., Wiedinmyer, C., Palmer, P. I., and Geron, C.: Estimates of global terrestrial isoprene emissions using MEGAN (Model of Emissions of Gases and Aerosols from Nature), Atmospheric Chemistry and Physics, 6, 3181–3210, https://doi.org/10.5194/acp-6-3181-2006, https://acp.copernicus.org/articles/6/3181/2006/, 2006.

Guenther, A. B., Jiang, X., Heald, C. L., Sakulyanontvittaya, T., Duhl, T., Emmons, L. K., and Wang, X.: The Model of Emissions of Gases and Aerosols from Nature version 2.1 (MEGAN2.1): an extended and updated framework for modeling biogenic emissions, Geoscientific Model Development, 5, 1471–1492, https://doi.org/10.5194/gmd-5-1471-2012, https://gmd.copernicus.org/articles/5/1471/2012/, 2012.

Hagemann, S. and Stacke, T.: Impact of the soil hydrology scheme on simulated soil moisture memory, Climate Dynamics, 44, 1731–1750, https://doi.org/10.1007/s00382-014-2221-6, 2015.

Hammer, M. S., van Donkelaar, A., Li, C., Lyapustin, A., Sayer, A. M., Hsu, N. C., Levy, R. C., Garay, M., Kalashnikova, O., Kahn, R. A., et al.: Global Estimates and Long-Term Trends of Fine Particulate Matter Concentrations (1998-2018), Environmental Science & Technology, 13, 7879–7890, 2020.

Hayes, P., Ortega, A., Cubison, M., Froyd, K., Zhao, Y., Cliff, S., Hu, W., Toohey, D., Flynn, J., Lefer, B., et al.: Organic aerosol composition and sources in Pasadena, California, during the 2010 CalNex campaign, Journal of Geophysical Research: Atmospheres, 118, 9233–9257, 2013.

Heald, C., Coe, H., Jimenez, J., Weber, R., Bahreini, R., Middlebrook, A., Russell, L., Jolleys, M., Fu, T.-M., Allan, J., et al.: Exploring the vertical profile of atmospheric organic aerosol: comparing 17 aircraft field campaigns with a global model, Atmospheric Chemistry and Physics, 11, 12 673–12 696, 2011.

Heald, C. L. and Kroll, J. H.: The fuel of atmospheric chemistry: Toward a complete description of reactive organic carbon, Science Advances, 6, https://doi.org/10.1126/sciadv.aay8967, https://advances.sciencemag.org/content/6/6/eaay8967, 2020.

Heald, C. L., Jacob, D. J., Park, R. J., Russell, L. M., Huebert, B. J., Seinfeld, J. H., Liao, H., and Weber, R. J.: A large organic aerosol source in the free troposphere missing from current models, Geophysical Research Letters, 32, https://doi.org/10.1029/2005GL023831, https://agupubs.onlinelibrary.wiley.com/doi/abs/10.1029/2005GL023831, 2005.

Hens, K., Novelli, A., Martinez, M., Auld, J., Axinte, R., Bohn, B., Fischer, H., Keronen, P., Kubistin, D., Nölscher, A. C., Oswald, R., Paasonen, P., Petäjä, T., Regelin, E., Sander, R., Sinha, V., Sipilä, M., Taraborrelli, D., Tatum Ernest, C., Williams, J., Lelieveld, J., and Harder, H.: Observation and modelling of HO_x radicals in a boreal forest, Atmospheric Chemistry and Physics, 14, 8723–8747, https://doi.org/10.5194/acp-14-8723-2014, https://acp.copernicus.org/articles/14/8723/2014/, 2014.

925 Holben, B., Eck, T., Slutsker, I., Tanre, D., Buis, J., Setzer, A., Vermote, E., Reagan, J., Kaufman, Y., Nakajima, T., et al.: AERONET: federated instrument network and data archive for aerosol characterization, Remote Sensing of Environment, 66, 1–16, 1998.

Hsu, N., Tsay, S.-C., King, M., and Herman, J.: Aerosol properties over bright-reflecting source regions, IEEE Transactions on Geoscience and Remote Sensing, 42, 557–569, https://doi.org/10.1109/TGRS.2004.824067, 2004.

Huey, L., Nowak, J., Tanner, D., and Kim, S.: ATom: L2 In Situ Peroxyacetyl Nitrate (PAN) Measurements from Georgia Tech CIMS,
930 https://doi.org/10.3334/ORNLDAAC/1715, https://daac.ornl.gov/cgi-bin/dsviewer.pl?ds_id=1715, 2019.

Huijnen, V., Pozzer, A., Arteta, J., Brasseur, G., Bouarar, I., Chabrillat, S., Christophe, Y., Doumbia, T., Flemming, J., Guth, J., Josse, B., Karydis, V. A., Marécal, V., and Pelletier, S.: Quantifying uncertainties due to chemistry modelling – evaluation of tropospheric composition simulations in the CAMS model (cycle 43R1), Geoscientific Model Development, 12, 1725–1752, https://doi.org/10.5194/gmd-12-1725-2019, https://gmd.copernicus.org/articles/12/1725/2019/, 2019.

935 Inness, A., Baier, F., Benedetti, A., Bouarar, I., Chabrillat, S., Clark, H., Clerbaux, C., Coheur, P., Engelen, R., Errera, Q., et al.: The MACC reanalysis: an 8-yr data set of atmospheric composition., Atmospheric Chemistry & Physics Discussions, 12, 2012.

Jacob, D., Field, B., Jin, E., Bey, I., Li, Q., Logan, J., and Yantosca, R.: Atmospheric budget of acetone, Journal of Geophysical Research: Atmospheres, 107, 4100, doi:10.1029/2001JD000 694, 2002.

Jacob, D. J., Field, B. D., Li, Q., Blake, D. R., de Gouw, J., Warneke, C., Hansel, A., Wisthaler, A., Singh, H. B., and Guenther,
940 A.: Global budget of methanol: Constraints from atmospheric observations, Journal of Geophysical Research: Atmospheres, 110, doi:10.1029/2004JD005 172, 2005.

Janssen, R., Tsimpidi, A., Karydis, V., Pozzer, A., Lelieveld, J., Crippa, M., Prévôt, A., Ait-Helal, W., Borbon, A., Sauvage, S., et al.: Influence of local production and vertical transport on the organic aerosol budget over Paris, Journal of Geophysical Research: Atmospheres, 122, 8276–8296, 2017.

945 Jenkin, M. E., Saunders, S. M., Wagner, V., and Pilling, M. J.: Protocol for the development of the Master Chemical Mechanism, MCM v3 (Part B): tropospheric degradation of aromatic volatile organic compounds, Atmospheric Chemistry and Physics, 3, 181–193, https://doi.org/10.5194/acp-3-181-2003, https://acp.copernicus.org/articles/3/181/2003/, 2003.

Jeuken, A., Siegmund, P., Heijboer, L., Feichter, J., and Bengtsson, L.: On the potential assimilating meteorological analyses in a global model for the purpose of model validation, Journal of Geophysical Research: Atmospheres, 101, 16 939–16 950, 1996.

950 Jo, D., Park, R., Kim, M., and Spracklen, D.: Effects of chemical aging on global secondary organic aerosol using the volatility basis set approach, Atmospheric Environment, 81, 230–244, 2013.

Jöckel, P., Tost, H., Pozzer, A., Brühl, C., Bucholz, J., L., G., Hoor, P., Kerkweg, A., Lawrence, M., Sander, R., Steil, B., Stiller, G., Tanarhte, M., Taraborrelli, D., van Aardenne, J., and Lelieveld, J.: Evaluation of the atmospheric chemistry GCM ECHAM5/MESSy: Consistent simulation of ozone in the stratosphere and troposphere, Atmos. Chem. Phys., 6, 5067–5104, 2006.

955 Jöckel, P., Kerkweg, A., Pozzer, A., Sander, R., Tost, H., Riede, H., Baumgaertner, A., Gromov, S., and Kern, B.: Development cycle 2 of the Modular Earth Submodel System (MESSy2), Geoscientific Model Development, 3, 717–752, https://doi.org/10.5194/gmd-3-717-2010, https://gmd.copernicus.org/articles/3/717/2010/, 2010.

Jöckel, P., Tost, H., Pozzer, A., Kunze, M., Kirner, O., Brenninkmeijer, C. A. M., Brinkop, S., Cai, D. S., Dyroff, C., Eckstein, J., Frank, F., Garny, H., Gottschaldt, K.-D., Graf, P., Grewe, V., Kerkweg, A., Kern, B., Matthes, S., Mertens, M., Meul, S., Neumaier, M., Nützel,
960 M., Oberländer-Hayn, S., Ruhnke, R., Runde, T., Sander, R., Scharffe, D., and Zahn, A.: Earth System Chemistry integrated Modelling (ESCiMo) with the Modular Earth Submodel System (MESSy) version 2.51, Geoscientific Model Development, 9, 1153–1200, https://doi.org/10.5194/gmd-9-1153-2016, https://gmd.copernicus.org/articles/9/1153/2016/, 2016.

Kaiser, J., Heil, A., Andreae, M., Benedetti, A., Chubarova, N., Jones, L., Morcrette, J.-J., Razinger, M., Schultz, M., Suttie, M., et al.: Biomass burning emissions estimated with a global fire assimilation system based on observed fire radiative power, Biogeosciences, 9, 527, 2012.

Karl, T., Potosnak, M., Guenther, A., Clark, D., Walker, J., Herrick, J. D., and Geron, C.: Exchange processes of volatile organic compounds above a tropical rain forest: Implications for modeling tropospheric chemistry above dense vegetation, Journal of Geophysical Research: Atmospheres, 109, https://doi.org/https://doi.org/10.1029/2004JD004738, https://agupubs.onlinelibrary.wiley.com/doi/abs/10.1029/2004JD004738, 2004.

Karydis, V., Tsimpidi, A., Pozzer, A., Astitha, M., and Lelieveld, J.: Effects of mineral dust on global atmospheric nitrate concentrations, Atmospheric Chemistry and Physics, 16, 1491–1509, 2016.

Kerkweg, A., Buchholz, J., Ganzeveld, L., Pozzer, A., Tost, H., and Jöckel, P.: Technical Note: An implementation of the dry removal processes DRY DEPosition and SEDImentation in the Modular Earth Submodel System (MESSy), Atmos. Chem. Phys., 6, 4617–4632, https://doi.org/https://doi.org/10.5194/gmd-14-495-2021, 2006a.

Kerkweg, A., Sander, R., Tost, H., and Jöckel, P.: Technical note: Implementation of prescribed (OFFLEM), calculated (ONLEM), and pseudo-emissions (TNUDGE) of chemical species in the Modular Earth Submodel System (MESSy), Atmos. Chem. Phys., 6, 3603–3609, https://doi.org/10.5194/acp-6-3603-2006, https://www.atmos-chem-phys.net/6/3603/2006/, 2006b.

Khan, M., Cooke, M., Utembe, S., Archibald, A., Maxwell, P., Morris, W., Xiao, P., Derwent, R., Jenkin, M., Percival, C., Walsh, R., Young, T., Simmonds, P., Nickless, G., O'Doherty, S., and Shallcross, D.: A study of global atmospheric budget and distribution of acetone using global atmospheric model STOCHEM-CRI, Atmospheric Environment, 112, 269–277, https://doi.org/https://doi.org/10.1016/j.atmosenv.2015.04.056, https://www.sciencedirect.com/science/article/pii/S1352231015300595, 2015.

Khan, M. A. H., Lyons, K., Chhantyal-Pun, R., McGillen, M. R., Caravan, R. L., Taatjes, C. A., Orr-Ewing, A. J., Percival, C. J., and Shallcross, D. E.: Investigating the Tropospheric Chemistry of Acetic Acid Using the Global 3-D Chemistry Transport Model, STOCHEM-CRI, Journal of Geophysical Research: Atmospheres, 123, 6267–6281, https://doi.org/10.1029/2018jd028529, 2018.

Klingmüller, K., Metzger, S., Abdelkader, M., Karydis, V. A., Stenchikov, G. L., Pozzer, A., and Lelieveld, J.: Revised mineral dust emissions in the atmospheric chemistry–climate model EMAC (MESSy 2.52 DU_Astitha1 KKDU2017 patch), Geoscientific Model Development, 11, 989–1008, https://doi.org/10.5194/gmd-11-989-2018, https://www.geosci-model-dev.net/11/989/2018/, 2018.

Kodros, J. K., Papanastasiou, D. K., Paglione, M., Masiol, M., Squizzato, S., Florou, K., Skyllakou, K., Kaltsonoudis, C., Nenes, A., and Pandis, S. N.: Rapid dark aging of biomass burning as an overlooked source of oxidized organic aerosol, Proceedings of the National Academy of Sciences, 117, 33 028–33 033, 2020.

Lana, A., Bell, T., Simó, R., Vallina, S., Ballabrera-Poy, J., Kettle, A., Dachs, J., Bopp, L., Saltzman, E., Stefels, J., et al.: An updated climatology of surface dimethlysulfide concentrations and emission fluxes in the global ocean, Global Biogeochemical Cycles, 25, 2011.

Laskin, A., Laskin, J., and Nizkorodov, S. A.: Chemistry of Atmospheric Brown Carbon, Chemical Reviews, 115, 4335–4382, https://doi.org/10.1021/cr5006167, https://doi.org/10.1021/cr5006167, publisher: American Chemical Society, 2015.

Lauer, A., Eyring, V., Hendricks, J., Jöckel, P., and Lohmann, U.: Global model simulations of the impact of ocean-going ships on aerosols, clouds, and the radiation budget, Atmos. Chem. Phys., 7, 5061–5079, https://doi.org/10.5194/acp-7-5061-2007, http://www.atmos-chem-phys.net/7/5061/2007/, 2007.

Lei, X., Chen, D., Wang, W., Liu, F., and Wang, W.: Quantum chemical studies of the OH-initiated oxidation reactions of propenols in the presence of O2, Molecular Physics, 117, 682–692, https://doi.org/10.1080/00268976.2018.1537527, 2018.

Lelieveld, J., Gromov, S., Pozzer, A., and Taraborrelli, D.: Global tropospheric hydroxyl distribution, budget and reactivity, Atmospheric Chemistry and Physics, 16, 12 477–12 493, https://doi.org/10.5194/acp-16-12477-2016, 2016.

Lelieveld, J., Bourtsoukidis, E., Brühl, C., Fischer, H., Fuchs, H., Harder, H., Hofzumahaus, A., Holland, F., Marno, D., Neumaier, M., et al.: The South Asian monsoon—pollution pump and purifier, Science, 361, 270–273, 2018.

1005   Li, H., Väliranta, M., Mäki, M., Kohl, L., Sannel, A. B. K., Pumpanen, J., Koskinen, M., Bäck, J., and Bianchi, F.: Overlooked organic vapor emissions from thawing Arctic permafrost, Environmental Research Letters, 15, 104 097, https://doi.org/10.1088/1748-9326/abb62d, https://doi.org/10.1088/1748-9326/abb62d, 2020.

Li, J.-L., Zhai, X., Wu, Y.-C., Wang, J., Zhang, H.-H., and Yang, G.-P.: Emissions and potential controls of light alkenes from the marginal seas of China, Science of The Total Environment, 758, 143 655, 2021.

1010   Li, Y., Pöschl, U., and Shiraiwa, M.: Molecular corridors and parameterizations of volatility in the chemical evolution of organic aerosols, Atmos. Chem. Phys, 16, 3327–3344, 2016.

Mahieu, E., Fischer, E. V., Franco, B., Palm, M., Wizenberg, T., Smale, D., Clarisse, L., Clerbaux, C., Coheur, P.-F., Hannigan, J. W., et al.: First retrievals of peroxyacetyl nitrate (PAN) from ground-based FTIR solar spectra recorded at remote sites, comparison with model and satellite data, Elem Sci Anth, 9, 00 027, 2021.

1015   Mallik, C., Tomsche, L., Bourtsoukidis, E., Crowley, J. N., Derstroff, B., Fischer, H., Hafermann, S., Hüser, I., Javed, U., Keßel, S., Lelieveld, J., Martinez, M., Meusel, H., Novelli, A., Phillips, G. J., Pozzer, A., Reiffs, A., Sander, R., Taraborrelli, D., Sauvage, C., Schuladen, J., Su, H., Williams, J., and Harder, H.: Oxidation processes in the eastern Mediterranean atmosphere: evidence from the modelling of HO_x measurements over Cyprus, Atmospheric Chemistry and Physics, 18, 10 825–10 847, https://doi.org/10.5194/acp-18-10825-2018, https://acp.copernicus.org/articles/18/10825/2018/, 2018.

1020   Mann, G. W., Carslaw, K. S., Spracklen, D. V., Ridley, D. A., Manktelow, P. T., Chipperfield, M. P., Pickering, S. J., and Johnson, C. E.: Description and evaluation of GLOMAP-mode: a modal global aerosol microphysics model for the UKCA composition-climate model, Geosci. Model Dev., 3, 519–551, https://doi.org/10.5194/gmd-3-519-2010, http://www.geosci-model-dev.net/3/519/2010/, 2010.

Martin, S., Artaxo, P., Chen, Q., Guenther, A., Gunthe, S., Jimenez, J., Manzi, A., Prenni, K., Pöschl, U., Schneider, J., and Swietlicki, E.: AMAZE-08 Aerosol Characterization and Meteorological Data, Central Amazon Basin: 2008, https://doi.org/10.3334/ORNLDAAC/1308,
1025   http://daac.ornl.gov/cgi-bin/dsviewer.pl?ds_id=1308, 2016.

McKain, K. and Sweeney, C.: ATom: CO2, CH4, and CO Measurements from Picarro, 2016-2018, https://doi.org/10.3334/ORNLDAAC/1732, https://daac.ornl.gov/cgi-bin/dsviewer.pl?ds_id=1732, 2021.

Miao, R., Chen, Q., Zheng, Y., Cheng, X., Sun, Y., Palmer, P. I., Shrivastava, M., Guo, J., Zhang, Q., Liu, Y., Tan, Z., Ma, X., Chen, S., Zeng, L., Lu, K., and Zhang, Y.: Model bias in simulating major chemical components of $PM_{2.5}$ in China, Atmospheric Chemistry and Physics,
1030   20, 12 265–12 284, https://doi.org/10.5194/acp-20-12265-2020, https://acp.copernicus.org/articles/20/12265/2020/, 2020.

Miao, R., Chen, Q., Shrivastava, M., Chen, Y., Zhang, L., Hu, J., Zheng, Y., and Liao, K.: Process-based and observation-constrained SOA simulations in China: the role of semivolatile and intermediate-volatility organic compounds and OH levels, Atmospheric Chemistry and Physics, 21, 16 183–16 201, 2021.

Millet, D. B., Jacob, D. J., Custer, T. G., de Gouw, J. A., Goldstein, A. H., Karl, T., Singh, H. B., Sive, B. C., Talbot, R. W., Warneke, C.,
1035   and Williams, J.: New constraints on terrestrial and oceanic sources of atmospheric methanol, Atmospheric Chemistry and Physics, 8, 6887–6905, https://doi.org/10.5194/acp-8-6887-2008, 2008.

Millet, D. B., Guenther, A., Siegel, D. A., Nelson, N. B., Singh, H. B., de Gouw, J. A., Warneke, C., Williams, J., Eerdekens, G., Sinha, V., Karl, T., Flocke, F., Apel, E., Riemer, D. D., Palmer, P. I., and Barkley, M.: Global atmospheric budget of acetaldehyde: 3-D model analysis

and constraints from in-situ and satellite observations, Atmospheric Chemistry and Physics, 10, 3405–3425, https://doi.org/10.5194/acp-10-3405-2010, 2010.

Millet, D. B., Baasandorj, M., Farmer, D. K., Thornton, J. A., Baumann, K., Brophy, P., Chaliyakunnel, S., de Gouw, J. A., Graus, M., Hu, L., Koss, A., Lee, B. H., Lopez-Hilfiker, F. D., Neuman, J. A., Paulot, F., Peischl, J., Pollack, I. B., Ryerson, T. B., Warneke, C., Williams, B. J., and Xu, J.: A large and ubiquitous source of atmospheric formic acid, Atmospheric Chemistry and Physics, 15, 6283–6304, https://doi.org/10.5194/acp-15-6283-2015, 2015.

Misztal, P. K., Hewitt, C. N., Wildt, J., Blande, J. D., Eller, A. S., Fares, S., Gentner, D. R., Gilman, J., Graus, M., Greenberg, J., et al.: Atmospheric benzenoid emissions from plants rival those from fossil fuels, Scientific reports, 5, 1–10, 2015.

Mohr, C., DeCarlo, P., Heringa, M., Chirico, R., Slowik, J., Richter, R., Reche, C., Alastuey, A., Querol, X., Seco, R., et al.: Identification and quantification of organic aerosol from cooking and other sources in Barcelona using aerosol mass spectrometer data, Atmospheric Chemistry and Physics, 12, 1649–1665, 2012.

Moreno, T., Querol, X., Castillo, S., Alastuey, A., Cuevas, E., Herrmann, L., Mounkaila, M., Elvira, J., and Gibbons, W.: Geochemical variations in aeolian mineral particles from the Sahara–Sahel Dust Corridor, Chemosphere, 65, 261 – 270, https://doi.org/https://doi.org/10.1016/j.chemosphere.2006.02.052, http://www.sciencedirect.com/science/article/pii/S0045653506002529, 2006.

Müller, J.-F., Liu, Z., Nguyen, V. S., Stavrakou, T., Harvey, J. N., and Peeters, J.: The reaction of methyl peroxy and hydroxyl radicals as a major source of atmospheric methanol, Nature Communications, 7, 13 213, https://doi.org/10.1038/ncomms13213, 2016.

Müller, J.-F., Stavrakou, T., Bauwens, M., Compernolle, S., and Peeters, J.: Chemistry and deposition in the Model of Atmospheric composition at Global and Regional scales using Inversion Techniques for Trace gas Emissions (MAGRITTE v1.0). Part B. Dry deposition, Geoscientific Model Development Discussions, 2018, 1–49, https://doi.org/10.5194/gmd-2018-317, https://gmd.copernicus.org/preprints/gmd-2018-317/, 2018.

Ng, N. L., Canagaratna, M. R., Zhang, Q., Jimenez, J. L., Tian, J., Ulbrich, I. M., Kroll, J. H., Docherty, K. S., Chhabra, P. S., Bahreini, R., Murphy, S. M., Seinfeld, J. H., Hildebrandt, L., Donahue, N. M., DeCarlo, P. F., Lanz, V. A., Prévôt, A. S. H., Dinar, E., Rudich, Y., and Worsnop, D. R.: Organic aerosol components observed in Northern Hemispheric datasets from Aerosol Mass Spectrometry, Atmospheric Chemistry and Physics, 10, 4625–4641, https://doi.org/10.5194/acp-10-4625-2010, https://acp.copernicus.org/articles/10/4625/2010/, 2010.

Nguyen, T. L., Peeters, J., and Vereecken, L.: Theoretical study of the gas-phase ozonolysis of β-pinene (C10H16), Phys. Chem. Chem. Phys., 11, 5643–5656, https://doi.org/10.1039/B822984H, http://dx.doi.org/10.1039/B822984H, 2009.

Nölscher, A., Butler, T., Auld, J., Veres, P., Muñoz, A., Taraborrelli, D., Vereecken, L., Lelieveld, J., and Williams, J.: Using total OH reactivity to assess isoprene photooxidation via measurement and model, Atmospheric Environment, 89, 453–463, https://doi.org/10.1016/j.atmosenv.2014.02.024, 2014.

Novelli, A., Vereecken, L., Bohn, B., Dorn, H.-P., Gkatzelis, G. I., Hofzumahaus, A., Holland, F., Reimer, D., Rohrer, F., Rosanka, S., Taraborrelli, D., Tillmann, R., Wegener, R., Yu, Z., Kiendler-Scharr, A., Wahner, A., and Fuchs, H.: Importance of isomerization reactions for OH radical regeneration from the photo-oxidation of isoprene investigated in the atmospheric simulation chamber SAPHIR, Atmospheric Chemistry and Physics, 20, 3333–3355, https://doi.org/10.5194/acp-20-3333-2020, https://acp.copernicus.org/articles/20/3333/2020/, 2020.

1075   Paglione, M., Gilardoni, S., Rinaldi, M., Decesari, S., Zanca, N., Sandrini, S., Giulianelli, L., Bacco, D., Ferrari, S., Poluzzi, V., et al.: The impact of biomass burning and aqueous-phase processing on air quality: a multi-year source apportionment study in the Po Valley, Italy, Atmospheric Chemistry and Physics, 20, 1233–1254, 2020.

Pai, S. J., Heald, C. L., Pierce, J. R., Farina, S. C., Marais, E. A., Jimenez, J. L., Campuzano-Jost, P., Nault, B. A., Middlebrook, A. M., Coe, H., et al.: An evaluation of global organic aerosol schemes using airborne observations, Atmospheric Chemistry and Physics, 20,
1080   2637–2665, 2020.

Patra, P. K., Krol, M. C., Montzka, S. A., Arnold, T., Atlas, E. L., Lintner, B. R., Stephens, B. B., Xiang, B., Elkins, J. W., Fraser, P. J., Ghosh, A., Hintsa, E. J., Hurst, D. F., Ishijima, K., Krummel, P. B., Miller, B. R., Miyazaki, K., Moore, F. L., Mühle, J., O'Doherty, S., Prinn, R. G., Steele, L. P., Takigawa, M., Wang, H. J., Weiss, R. F., Wofsy, S. C., and Young, D.: Observational evidence for interhemispheric hydroxyl-radical parity, Nature, 513, 219–223, https://doi.org/10.1038/nature13721, 2014.

1085   Paulot, F., Wunch, D., Crounse, J. D., Toon, G. C., Millet, D. B., DeCarlo, P. F., Vigouroux, C., Deutscher, N. M., Abad, G. G., Notholt, J., Warneke, T., Hannigan, J. W., Warneke, C., de Gouw, J. A., Dunlea, E. J., Mazière, M. D., Griffith, D. W. T., Bernath, P., Jimenez, J. L., and Wennberg, P. O.: Importance of secondary sources in the atmospheric budgets of formic and acetic acids, Atmospheric Chemistry and Physics, 11, 1989–2013, https://doi.org/10.5194/acp-11-1989-2011, 2011.

Pollmann, J., Helmig, D., Hueber, J., Plass-Dülmer, C., and Tans, P.: Sampling, storage, and analysis of C2–C7 non-methane hydrocarbons
1090   from the US National Oceanic and Atmospheric Administration Cooperative Air Sampling Network glass flasks, Journal of Chromatography A, 1188, 75–87, 2008.

Pöschl, U., Von Kuhlmann, R., Poisson, N., and Crutzen, P. J.: Development and intercomparison of condensed isoprene oxidation mechanisms for global atmospheric modeling, Journal of Atmospheric Chemistry, 37, 29–52, https://doi.org/10.1023/A:1006391009798, 2000.

Pozzer, A., Jöckel, P., Sander, R., Williams, J., Ganzeveld, L., and Lelieveld, J.: Technical Note: The MESSy-submodel AIRSEA cal-
1095   culating the air-sea exchange of chemical species, Atmos. Chem. Phys., 6, 5435–5444, https://doi.org/10.5194/acp-6-5435-2006, http://www.atmos-chem-phys.net/6/5435/2006/, 2006.

Pozzer, A., Jöckel, P., Tost, H., Sander, R., Ganzeveld, L., Kerkweg, A., and Lelieveld, J.: Simulating organic species with the global atmospheric chemistry general circulation model ECHAM5/MESSy1: a comparison of model results with observations, Atmospheric Chemistry and Physics, 7, 2527–2550, https://doi.org/10.5194/acp-7-2527-2007, https://acp.copernicus.org/articles/7/2527/2007/, 2007.

1100   Pozzer, A., Jöckel, P., and Van Aardenne, J.: The influence of the vertical distribution of emissions on tropospheric chemistry, Atmospheric Chemistry and Physics, 9, 9417–9432, https://doi.org/10.5194/acp-9-9417-2009, https://www.atmos-chem-phys.net/9/9417/2009/, 2009.

Pozzer, A., Pollmann, J., Taraborrelli, D., Jöckel, P., Helmig, D., Tans, P., Hueber, J., and Lelieveld, J.: Observed and simulated global distribution and budget of atmospheric C_2-C_5 alkanes, Atmos. Chem. Phys., 10, 4403–4422, https://doi.org/10.5194/acp-10-4403-2010, http://www.atmos-chem-phys.net/10/4403/2010/, 2010.

1105   Pozzer, A., de Meij, A., Pringle, K. J., Tost, H., Doering, U. M., van Aardenne, J., and Lelieveld, J.: Distributions and regional budgets of aerosols and their precursors simulated with the EMAC chemistry-climate model, Atmos. Chem. Phys., 12, 961–987, https://doi.org/10.5194/acp-12-961-2012, http://www.atmos-chem-phys.net/12/961/2012/, 2012a.

Pozzer, A., Zimmermann, P., Doering, U., van Aardenne, J., Tost, H., Dentener, F., Janssens-Maenhout, G., and Lelieveld, J.: Effects of business-as-usual anthropogenic emissions on air quality, Atmos. Chem. Phys., 12, 6915–6937, https://doi.org/10.5194/acp-12-6915-
1110   2012, http://www.atmos-chem-phys.net/12/6915/2012/, 2012b.

Pozzer, A., Tsimpidi, A. P., Karydis, V. A., de Meij, A., and Lelieveld, J.: Impact of agricultural emission reductions on fine-particulate matter and public health, Atmospheric Chemistry and Physics, 17, 12 813–12 826, https://doi.org/10.5194/acp-17-12813-2017, https://acp.copernicus.org/articles/17/12813/2017/, 2017.

Pringle, K. J., Tost, H., Metzger, S., Steil, B., Giannadaki, D., Nenes, A., Fountoukis, C., Stier, P., Vignati, E., and Lelieveld, J.: Description and evaluation of GMXe: a new aerosol submodel for global simulations (v1), Geosci. Model Dev., 3, 391–412, https://doi.org/10.5194/gmd-3-391-2010, http://www.geosci-model-dev.net/3/391/2010/, 2010a.

Pringle, K. J., Tost, H., Pozzer, A., Pöschl, U., and Lelieveld, J.: Global distribution of the effective aerosol hygroscopicity parameter for CCN activation, Atmos. Chem. Phys., 10, 5241–5255, https://doi.org/10.5194/acp-10-5241-2010, http://www.atmos-chem-phys.net/10/5241/2010/, 2010b.

Ramo, R., Roteta, E., Bistinas, I., van Wees, D., Bastarrika, A., Chuvieco, E., and van der Werf, G. R.: African burned area and fire carbon emissions are strongly impacted by small fires undetected by coarse resolution satellite data, Proceedings of the National Academy of Sciences, 118, https://doi.org/10.1073/pnas.2011160118, https://www.pnas.org/content/118/9/e2011160118, 2021.

Reid, E. A., Reid, J. S., Meier, M. M., Dunlap, M. R., Cliff, S. S., Broumas, A., Perry, K., and Maring, H.: Characterization of African dust transported to Puerto Rico by individual particle and size segregated bulk analysis, Journal of Geophysical Research: Atmospheres, 108, https://doi.org/https://doi.org/10.1029/2002JD002935, https://agupubs.onlinelibrary.wiley.com/doi/abs/10.1029/2002JD002935, 2003.

Roeckner, E., Brokopf, R., Esch, M., Giorgetta, M., Hagemann, S., Kornblueh, L., Manzini, E., Schlese, U., and Schulzweida, U.: Sensitivity of simulated climate to horizontal and vertical resolution in the ECHAM5 atmosphere model, Journal of Climate, 19, 3771–3791, 2006.

Rosanka, S., Vu, G. H. T., Nguyen, H. M. T., Pham, T. V., Javed, U., Taraborrelli, D., and Vereecken, L.: Atmospheric chemical loss processes of isocyanic acid (HNCO): a combined theoretical kinetic and global modelling study, Atmospheric Chemistry and Physics, 20, 6671–6686, https://doi.org/10.5194/acp-20-6671-2020, https://acp.copernicus.org/articles/20/6671/2020/, 2020.

Rosanka, S., Franco, B., Clarisse, L., Coheur, P.-F., Pozzer, A., Wahner, A., and Taraborrelli, D.: The impact of organic pollutants from Indonesian peatland fires on the tropospheric and lower stratospheric composition, Atmospheric Chemistry and Physics, 21, 11 257–11 288, https://doi.org/10.5194/acp-21-11257-2021, https://acp.copernicus.org/articles/21/11257/2021/, 2021a.

Rosanka, S., Sander, R., Franco, B., Wespes, C., Wahner, A., and Taraborrelli, D.: Oxidation of low-molecular-weight organic compounds in cloud droplets: global impact on tropospheric oxidants, Atmospheric Chemistry and Physics, 21, 9909–9930, https://doi.org/10.5194/acp-21-9909-2021, https://acp.copernicus.org/articles/21/9909/2021/, 2021b.

Rosanka, S., Sander, R., Wahner, A., and Taraborrelli, D.: Oxidation of low-molecular-weight organic compounds in cloud droplets: development of the Jülich Aqueous-phase Mechanism of Organic Chemistry (JAMOC) in CAABA/MECCA (version 4.5.0), Geoscientific Model Development, 14, 4103–4115, https://doi.org/10.5194/gmd-14-4103-2021, https://gmd.copernicus.org/articles/14/4103/2021/, 2021c.

Ryerson, T., Thompson, C., Peischl, J., and Bourgeois, I.: ATom: L2 In Situ Measurements from NOAA Nitrogen Oxides and Ozone (NOyO3) Instrument, https://doi.org/10.3334/ORNLDAAC/1734, https://daac.ornl.gov/cgi-bin/dsviewer.pl?ds_id=1734, 2019.

Saikawa, E., Kim, H., Zhong, M., Avramov, A., Zhao, Y., Janssens-Maenhout, G., Kurokawa, J.-i., Klimont, Z., Wagner, F., Naik, V., et al.: Comparison of emissions inventories of anthropogenic air pollutants and greenhouse gases in China, Atmospheric Chemistry and Physics, 17, 6393–6421, 2017.

Sander, R.: Compilation of Henry's law constants (version 4.0) for water as solvent, Atmospheric Chemistry and Physics, 15, 4399–4981, https://doi.org/10.5194/acp-15-4399-2015, https://acp.copernicus.org/articles/15/4399/2015/, 2015.

Sander, R., Baumgaertner, A., Cabrera-Perez, D., Frank, F., Gromov, S., Grooß, J.-U., Harder, H., Huijnen, V., Jöckel, P., Karydis, V. A., Niemeyer, K. E., Pozzer, A., Riede, H., Schultz, M. G., Taraborrelli, D., and Tauer, S.: The community atmospheric chem-

istry box model CAABA/MECCA-4.0, Geoscientific Model Development, 12, 1365–1385, https://doi.org/10.5194/gmd-12-1365-2019, https://gmd.copernicus.org/articles/12/1365/2019/, 2019.

Schaap, M.: On the importance of aerosol nitrate over Europe : data analysis and modelling, Ph.D. thesis, Universiteit Utrecht, Nederland, https://dspace.library.uu.nl/handle/1874/708, 2003.

Schaap, M., van Loon, M., ten Brink, H. M., Dentener, F. J., and Builtjes, P. J. H.: Secondary inorganic aerosol simulations for Europe with special attention to nitrate, Atmospheric Chemistry and Physics, 4, 857–874, https://doi.org/10.5194/acp-4-857-2004, https://acp.copernicus.org/articles/4/857/2004/, 2004.

Scholten, R. C., Jandt, R., Miller, E. A., Rogers, B. M., and Veraverbeke, S.: Overwintering fires in boreal forests, Nature, 593, 399–404, 2021.

Shiraiwa, M., Li, Y., Tsimpidi, A., Karydis, V., Berkemeier, T., Pandis, S., Lelieveld, J., Koop, T., and Pöschl, U.: Global distribution of particle phase state in atmospheric secondary organic aerosols, Nat. Commun., 8, 15002, 2017.

Singh, H. B., Chen, Y., Staudt, A., Jacob, D., Blake, D., Heikes, B., and Snow, J.: Evidence from the Pacific troposphere for large global sources of oxygenated organic compounds, Nature, 410, 1078–1081, https://doi.org/10.1038/35074067, 2001.

Stavrakou, T., Guenther, A., Razavi, A., Clarisse, L., Clerbaux, C., Coheur, P.-F., Hurtmans, D., Karagulian, F., Mazière, M. D., Vigouroux, C., Amelynck, C., Schoon, N., Laffineur, Q., Heinesch, B., Aubinet, M., Rinsland, C., and Müller, J.-F.: First space-based derivation of the global atmospheric methanol emission fluxes, Atmospheric Chemistry and Physics, 11, 4873–4898, https://doi.org/10.5194/acp-11-4873-2011, 2011.

Stavrakou, T., Müller, J.-F., Peeters, J., Razavi, A., Clarisse, L., Clerbaux, C., Coheur, P.-F., Hurtmans, D., Mazière, M. D., Vigouroux, C., Deutscher, N. M., Griffith, D. W. T., Jones, N., and Paton-Walsh, C.: Satellite evidence for a large source of formic acid from boreal and tropical forests, Nature Geoscience, 5, 26–30, https://doi.org/10.1038/ngeo1354, 2012.

Sun, Y.-L., Zhang, Q., Schwab, J., Demerjian, K., Chen, W.-N., Bae, M.-S., Hung, H.-M., Hogrefe, O., Frank, B., Rattigan, O., et al.: Characterization of the sources and processes of organic and inorganic aerosols in New York city with a high-resolution time-of-flight aerosol mass apectrometer, Atmospheric Chemistry and Physics, 11, 1581–1602, 2011.

Tadic, I., Nussbaumer, C. M., Bohn, B., Harder, H., Marno, D., Martinez, M., Obersteiner, F., Parchatka, U., Pozzer, A., Rohloff, R., Zöger, M., Lelieveld, J., and Fischer, H.: Central role of nitric oxide in ozone production in the upper tropical troposphere over the Atlantic Ocean and western Africa, Atmospheric Chemistry and Physics, 21, 8195–8211, https://doi.org/10.5194/acp-21-8195-2021, https://acp.copernicus.org/articles/21/8195/2021/, 2021.

Taraborrelli, D., Lawrence, M. G., Butler, T. M., Sander, R., and Lelieveld, J.: Mainz Isoprene Mechanism 2 (MIM2): an isoprene oxidation mechanism for regional and global atmospheric modelling, Atmospheric Chemistry and Physics, 9, 2751–2777, https://doi.org/10.5194/acp-9-2751-2009, https://acp.copernicus.org/articles/9/2751/2009/, 2009.

Taraborrelli, D., Lawrence, M. G., Crowley, J. N., Dillon, T. J., Gromov, S., Groß, C. B. M., Vereecken, L., and Lelieveld, J.: Hydroxyl radical buffered by isoprene oxidation over tropical forests, Nature Geoscience, 5, 190–193, https://doi.org/10.1038/ngeo1405, 2012.

Taraborrelli, D., Cabrera-Perez, D., Bacer, S., Gromov, S., Lelieveld, J., Sander, R., and Pozzer, A.: Influence of aromatics on tropospheric gas-phase composition, Atmospheric Chemistry and Physics, 21, 2615–2636, https://doi.org/10.5194/acp-21-2615-2021, https://acp.copernicus.org/articles/21/2615/2021/, 2021.

Tilmes, S., Lamarque, J.-F., Emmons, L. K., Kinnison, D. E., Marsh, D., Garcia, R. R., Smith, A. K., Neely, R. R., Conley, A., Vitt, F., et al.: Representation of the community earth system model (CESM1) CAM4-chem within the chemistry-climate model initiative (CCMI), Geoscientific Model Development, 9, 1853–1890, 2016.

Tost, H. and Pringle, K. J.: Improvements of organic aerosol representations and their effects in large-scale atmospheric models, Atmospheric Chemistry and Physics, 12, 8687–8709, https://doi.org/10.5194/acp-12-8687-2012, https://acp.copernicus.org/articles/12/8687/2012/, 2012.

Tost, H., Jöckel, P., Kerkweg, A., Sander, R., and Lelieveld, J.: Technical Note: A new comprehensive SCAVenging submodel for global atmospheric chemistry modelling, Atmos. Chem. Phys., 6, 565–574, 2006.

Tsimpidi, A. P., Karydis, V. A., Pozzer, A., Pandis, S. N., and Lelieveld, J.: ORACLE (v1.0): module to simulate the organic aerosol composition and evolution in the atmosphere, Geoscientific Model Development, 7, 3153–3172, https://doi.org/10.5194/gmd-7-3153-2014, https://gmd.copernicus.org/articles/7/3153/2014/, 2014.

Tsimpidi, A. P., Karydis, V. A., Pandis, S. N., and Lelieveld, J.: Global combustion sources of organic aerosols: model comparison with 84 AMS factor-analysis data sets, Atmospheric Chemistry and Physics, 16, 8939–8962, https://doi.org/10.5194/acp-16-8939-2016, https://acp.copernicus.org/articles/16/8939/2016/, 2016.

van der Werf, G. R., Randerson, J. T., Giglio, L., van Leeuwen, T. T., Chen, Y., Rogers, B. M., Mu, M., van Marle, M. J. E., Morton, D. C., Collatz, G. J., Yokelson, R. J., and Kasibhatla, P. S.: Global fire emissions estimates during 1997–2016, Earth System Science Data, 9, 697–720, https://doi.org/10.5194/essd-9-697-2017, 2017.

van Eijck, A., Opatz, T., Taraborrelli, D., Sander, R., and Hoffmann, T.: New tracer compounds for secondary organic aerosol formation from β-caryophyllene oxidation, Atmospheric Environment, 80, 122–130, https://doi.org/10.1016/J.ATMOSENV.2013.07.060, 2013.

Vereecken, L. and Peeters, J.: A theoretical study of the OH-initiated gas-phase oxidation mechanism of β-pinene ($C_{10}H_{16}$): first generation products, Phys. Chem. Chem. Phys., 14, 3802–3815, https://doi.org/10.1039/C2CP23711C, http://dx.doi.org/10.1039/C2CP23711C, 2012.

Vereecken, L., Müller, J.-F., and Peeters, J.: Low-volatility poly-oxygenates in the OH-initiated atmospheric oxidation of α-pinene: impact of non-traditional peroxyl radical chemistry, Phys. Chem. Chem. Phys., 9, 5241–5248, https://doi.org/10.1039/B708023A, http://dx.doi.org/10.1039/B708023A, 2007.

Vereecken, L., Novelli, A., and Taraborrelli, D.: Unimolecular decay strongly limits the atmospheric impact of Criegee intermediates, Phys. Chem. Chem. Phys., 19, 31 599–31 612, https://doi.org/10.1039/C7CP05541B, http://dx.doi.org/10.1039/C7CP05541B, 2017.

Veres, P., Neuman, J., and Ryerson, T.: ATom: L2 Measurements from NOAA ToF Chemical Ionization Mass Spectrometer, Version 2, https://doi.org/10.3334/ORNLDAAC/1921, https://daac.ornl.gov/cgi-bin/dsviewer.pl?ds_id=1921, 2021.

Vignati, E., Wilson, J., and Stier, P.: M7: An efficient size-resolved aerosol microphysics module for large-scale aerosol transport models, Journal of Geophysical Research: Atmospheres, 109, https://doi.org/10.1029/2003JD004485, 2004.

Wang, C., Yuan, T., Wood, S. A., Goss, K.-U., Li, J., Ying, Q., and Wania, F.: Uncertain Henry's law constants compromise equilibrium partitioning calculations of atmospheric oxidation products, Atmospheric Chemistry and Physics, 17, 7529–7540, https://doi.org/10.5194/acp-17-7529-2017, https://acp.copernicus.org/articles/17/7529/2017/, 2017.

Wang, S., Hornbrook, R. S., Hills, A., Emmons, L. K., Tilmes, S., Lamarque, J.-F., Jimenez, J. L., Campuzano-Jost, P., Nault, B. A., Crounse, J. D., Wennberg, P. O., Kim, M., Allen, H., Ryerson, T. B., Thompson, C. R., Peischl, J., Moore, F., Nance, D., Hall, B., Elkins, J., Tanner, D., Huey, L. G., Hall, S. R., Ullmann, K., Orlando, J. J., Tyndall, G. S., Flocke, F. M., Ray, E., Hanisco, T. F., Wolfe, G. M., Clair, J. S., Commane, R., Daube, B., Barletta, B., Blake, D. R., Weinzierl, B., Dollner, M., Conley, A., Vitt, F., Wofsy, S. C., Riemer, D. D., and Apel, E. C.: Atmospheric Acetaldehyde: Importance of Air-Sea Exchange and a Missing Source in the Remote Troposphere, Geophysical Research Letters, https://doi.org/10.1029/2019gl082034, 2019.

Weilenmann, M., Favez, J.-Y., and Alvarez, R.: Cold-start emissions of modern passenger cars at different low ambient temperatures and their evolution over vehicle legislation categories, Atmospheric environment, 43, 2419–2429, 2009.

Wesely, M.: Parameterization of surface resistances to gaseous dry deposition in regional-scale numerical models, Atmospheric Environment (1967), 23, 1293–1304, 1989.

Whitburn, S., Van Damme, M., Clarisse, L., Bauduin, S., Heald, C. L., Hadji-Lazaro, J., Hurtmans, D., Zondlo, M. A., Clerbaux, C., and Coheur, P.-F.: A flexible and robust neural network IASI-NH3 retrieval algorithm, Journal of Geophysical Research: Atmospheres, 121, 6581–6599, https://doi.org/10.1002/2016jd024828, 2016.

Wofsy, S., Afshar, S., Allen, H., Apel, E., Asher, E., Barletta, B., Bent, J., Bian, H., Biggs, B., Blake, D., Blake, N., Bourgeois, I., Brock, C., Brune, W., Budney, J., Bui, T., Butler, A., Campuzano-Jost, P., Chang, C., Chin, M., Commane, R., Correa, G., Crounse, J., Cullis, P. D., Daube, B., Day, D., Dean-Day, J., Dibb, J., DiGangi, J., Diskin, G., Dollner, M., Elkins, J., Erdesz, F., Fiore, A., Flynn, C., Froyd, K., Gesler, D., Hall, S., Hanisco, T., Hannun, R., Hills, A., Hintsa, E., Hoffman, A., Hornbrook, R., Huey, L., Hughes, S., Jimenez, J., Johnson, B., Katich, J., Keeling, R., Kim, M., Kupc, A., Lait, L., McKain, K., Mclaughlin, R., Meinardi, S., Miller, D., Montzka, S., Moore, F., Morgan, E., Murphy, D., Murray, L., Nault, B., Neuman, J., Newman, P., Nicely, J., Pan, X., Paplawsky, W., Peischl, J., Prather, M., Price, D., Ray, E., Reeves, J., Richardson, M., Rollins, A., Rosenlof, K., Ryerson, T., Scheuer, E., Schill, G., Schroder, J., Schwarz, J., St.Clair, J., Steenrod, S., Stephens, B., Strode, S., Sweeney, C., Tanner, D., Teng, A., Thames, A., Thompson, C., Ullmann, K., Veres, P., Wagner, N., Watt, A., Weber, R., Weinzierl, B., Wennberg, P., Williamson, C., Wilson, J., Wolfe, G., Woods, C., Zeng, L., and Vieznor, N.: ATom: Merged Atmospheric Chemistry, Trace Gases, and Aerosols, Version 2, https://doi.org/10.3334/ORNLDAAC/1925, https://daac.ornl.gov/cgi-bin/dsviewer.pl?ds_id=1925, 2021.

Wolfe, G. M., Nicely, J. M., St. Clair, J. M., Hanisco, T. F., Liao, J., Oman, L. D., Brune, W. B., Miller, D., Thames, A., González Abad, G., Ryerson, T. B., Thompson, C. R., Peischl, J., McKain, K., Sweeney, C., Wennberg, P. O., Kim, M., Crounse, J. D., Hall, S. R., Ullmann, K., Diskin, G., Bui, P., Chang, C., and Dean-Day, J.: Mapping hydroxyl variability throughout the global remote troposphere via synthesis of airborne and satellite formaldehyde observations, Proceedings of the National Academy of Sciences, 116, 11 171–11 180, https://doi.org/10.1073/pnas.1821661116, 2019.

Yáñez Serrano, A. M., Nölscher, A. C., Williams, J., Wolff, S., Alves, E., Martins, G. A., Bourtsoukidis, E., Brito, J., Jardine, K., Artaxo, P., and Kesselmeier, J.: Diel and seasonal changes of biogenic volatile organic compounds within and above an Amazonian rainforest, Atmospheric Chemistry and Physics, 15, 3359–3378, https://doi.org/10.5194/acp-15-3359-2015, https://acp.copernicus.org/articles/15/3359/2015/, 2015.

Yienger, J.: Empirical model of global soil-biogenic NOx emissions, J. Geophys. Res., 100, 464, 1995.

Zhao, B., Wang, S., Donahue, N. M., Jathar, S. H., Huang, X., Wu, W., Hao, J., and Robinson, A. L.: Quantifying the effect of organic aerosol aging and intermediate-volatility emissions on regional-scale aerosol pollution in China, Scientific reports, 6, 1–10, 2016.